

INFORMATION TO USERS

This manuscript has been reproduced from the microfilm master. UMI films the text directly from the original or copy submitted. Thus, some thesis and dissertation copies are in typewriter face, while others may be from any type of computer printer.

The quality of this reproduction is dependent upon the quality of the copy submitted. Broken or indistinct print, colored or poor quality illustrations and photographs, print bleedthrough, substandard margins, and improper alignment can adversely affect reproduction.

In the unlikely event that the author did not send UMI a complete manuscript and there are missing pages, these will be noted. Also, if unauthorized copyright material had to be removed, a note will indicate the deletion.

Oversize materials (e.g., maps, drawings, charts) are reproduced by sectioning the original, beginning at the upper left-hand corner and continuing from left to right in equal sections with small overlaps. Each original is also photographed in one exposure and is included in reduced form at the back of the book.

Photographs included in the original manuscript have been reproduced xerographically in this copy. Higher quality 6" x 9" black and white photographic prints are available for any photographs or illustrations appearing in this copy for an additional charge. Contact UMI directly to order.



Bell & Howell Information and Learning
300 North Zeeb Road, Ann Arbor, MI 48106-1346 USA
800-521-0600

An Eulerian 3D Analysis of Water Droplets Impingement
on a Convair-580 Nose and Cockpit Geometry

Ziad Boutanios

A Thesis
in
The Department
of
Mechanical Engineering

Presented in Partial Fulfillment of the Requirements
for the Degree of Master of Applied Science at
Concordia University
Montréal, Québec, Canada

April 1999

© Ziad Boutanios, 1999



National Library
of Canada

Acquisitions and
Bibliographic Services

395 Wellington Street
Ottawa ON K1A 0N4
Canada

Bibliothèque nationale
du Canada

Acquisitions et
services bibliographiques

395, rue Wellington
Ottawa ON K1A 0N4
Canada

Your file Votre référence

Our file Notre référence

The author has granted a non-exclusive licence allowing the National Library of Canada to reproduce, loan, distribute or sell copies of this thesis in microform, paper or electronic formats.

The author retains ownership of the copyright in this thesis. Neither the thesis nor substantial extracts from it may be printed or otherwise reproduced without the author's permission.

L'auteur a accordé une licence non exclusive permettant à la Bibliothèque nationale du Canada de reproduire, prêter, distribuer ou vendre des copies de cette thèse sous la forme de microfiche/film, de reproduction sur papier ou sur format électronique.

L'auteur conserve la propriété du droit d'auteur qui protège cette thèse. Ni la thèse ni des extraits substantiels de celle-ci ne doivent être imprimés ou autrement reproduits sans son autorisation.

0-612-39103-5

Abstract

An Eulerian 3D Analysis of Water Droplets Impingement on a Convair-580 Nose and Cockpit Geometry

Ziad Boutanios

This thesis consists of the first 3-D application of an Eulerian droplet impingement code. The code, DROP3D, was developed at the CFD Laboratory at Concordia University by Professor Yves Bourgault. DROP3D is part of an integrated in-flight icing package, FENSAP-ICE, under constant development at the CFD Laboratory allowing aerodynamic performance degradation and ice accretion analysis as well.

Code validation results in both 2-D and 3-D are presented and discussed. Results of a 3-D analysis over a Convair-580 nose and cockpit geometry are presented as well. This 3-D analysis is actually a simulation of a flight segment of the Canadian Freezing Drizzle Experiment as conducted by the Atmospheric Environment Services. Special emphasis is given to side window impingement on the Convair-580. The Eulerian approach's advantages over the classical Lagrangian approach are also discussed.

Acknowledgements

I would like to thank my supervisors Professors W.G. Habashi and Y. Bourgault for their continuous guidance, support, and encouragement throughout this research. I am especially grateful for their positive and attentive approach whenever I encountered a difficulty during my work.

Special thanks to Dr. Stewart Cober from Atmospheric Environment Services for all the help he provided as well as making available the Canadian Freezing Drizzle Experiment flight data.

Last but not least, the CFD Lab staff and student population who welcomed me in their special little community and helped me get acquainted with the Lab's computational environment and tools.

Contents

List of Figures	vii
List of Tables	x
1 Introduction	1
2 Physical Model	5
3 Computational Approach	10
3.1 Air Flow Code	10
3.2 Droplets Flow Code	11
3.2.1 Algorithmic Features	11
3.2.2 Discretization	12
3.2.3 Boundary Conditions	13
4 CAD Modeling and Meshing Techniques	14
5 Droplet Code Validation and Test Cases	19
5.1 2-D Test Case	19
5.2 3-D Test Case	20

6	Convair-580 Analysis	32
6.1	Convair-580 Air Flow Solution	32
6.2	Convair-580 Droplet Solutions	34
7	Conclusions and Future Work	47
7.1	Conclusions	47
7.2	Future Work	49
	Bibliography	50

List of Figures

4.1	Example of an input data file for the Convair-580 geometry	14
4.2	Convair-580 nose/cockpit geometry with its quarter-ellipsoid solution domain	15
4.3	Convair-580 nose/cockpit blocking	16
4.4	Convair-580 nose/cockpit Euler air flow solution structured mesh with 156095 nodes and hexahedral elements	17
4.5	Convair-580 nose/cockpit Euler air flow solution structured mesh on the aircraft body surface	18
5.1	Side view of the 2-D cylinder validation mesh	21
5.2	Inviscid pressure field around the 2-D cylinder geometry	22
5.3	Collection efficiency at the surface of a 2-D cylinder for a droplet diameter of $16\mu\text{m}$	22
5.4	Collection efficiency at the surface of a 2-D cylinder for a Langmuir-D distribution with an $\text{MVD} = 16\mu\text{m}$	23
5.5	Comparison of computed collection efficiency on the surface of the 2-D cylinder for the Langmuir distribution and the MVD solution to experi- mental data	23
5.6	Hexahedral mesh for the sphere test-cases	26
5.7	Closeup of a cut through the center of the sphere	27

5.8	15.04cm Sphere inviscid solution pressure field	27
5.9	15.04cm sphere surface collection efficiency for $d=5.8\mu m$ (left) and $d=9.7\mu m$ (right)	28
5.10	15.04cm sphere surface collection efficiency for $d=13.2\mu m$ (left) and $d=18.6\mu m$ (right)	28
5.11	15.04cm sphere surface collection efficiency for $d=25.5\mu m$ (left) and $d=32.4\mu m$ (right)	29
5.12	15.04cm sphere surface collection efficiency for $d=41.3\mu m$	29
5.13	15.04cm sphere surface collection efficiency for the combined solution (left) and the MVD = $18.6\mu m$ solution (right)	30
5.14	15.04cm sphere surface collection efficiency vs. distance from the stagna- tion point	31
6.1	Surface pressure profile and pressure contours along the Convair's plane of symmetry	34
6.2	Close-up of the surface pressure profile at the windows	35
6.3	Droplet diameter distribution measured during a CFDE flight	38
6.4	Front view of the Convair-580 surface collection efficiency for a droplet diameter of $10\mu m$ (left) and $13\mu m$ (right)	38
6.5	Front view of the Convair-580 surface collection efficiency for a droplet diameter of $20\mu m$ (left) and $50\mu m$ (right)	39
6.6	Front view of the Convair-580 surface collection efficiency for a droplet diameter of $100\mu m$ (left) and $200\mu m$ (right)	40
6.7	Front view of the Convair-580 surface collection efficiency for a droplet diameter of $300\mu m$ (left) and $400\mu m$ (right)	41

6.8	Front view of the Convair-580 surface collection efficiency for a droplet diameter of $1000\mu m$	42
6.9	Front view of the Convair-580 surface collection efficiency for the combined solution (left) and the $MVD = 174\mu m$ solution (right)	43
6.10	Vertical and horizontal cuts locations on the Convair-580 surface	43
6.11	Collection efficiencies on the Convair-580 surface along a vertical cut . . .	44
6.12	Collection efficiencies on the Convair-580 side window surface along a horizontal cut	45
6.13	Comparison of the in-flight ice patch shape to the Eulerian impingement profile on the nose of the Convair-580	46

List of Tables

5.1	Langmuir-D distribution of droplet diameters with an MVD of $16\mu\text{m}$ as used for the 2-D cylinder testcase	21
5.2	Langmuir-D distribution of droplet diameters with an MVD of $18.6\mu\text{m}$ as used for the 3-D sphere test-case	26
6.1	LWC weights for the droplet diameters chosen to discretize the AES in-flight distribution	36

Chapter 1

Introduction

Efficient in-flight de-anti-icing of an aircraft requires proper knowledge of Supercooled Water Droplet (SCWD) impingement profiles in icing conditions or knowledge of locations of ice formation on the aircraft. This is often monitored through visual inspection of local surface protuberances and discontinuities on the aircraft surface such as bolts and window recesses which are considered general indicators of icing accretion. The belief is that ice will form at such locations before, or simultaneously, with others such as lifting and aerodynamic control surfaces. There is no experimental or analytical proof to these practices which are after all highly speculative. Moreover experiments remain severely limited in covered range of operating conditions and tested aircraft geometries and extrapolation from existing data and empirical relations is neither easy nor always possible, let alone reliable.

The airframe icing problem was recognized as early as the mid 1940's and some research was initiated in the mid 1960's by the Federal Aviation Administration (FAA) in order to address the issue[1]. The work was carried out by General Dynamics engineers and covered some meteorological icing data statistics, physics of ice collection, methods of protection including de/anti-icing, applications to different types of aircraft including rotary wing, ice detectors and controls, and testing of aircraft and ice protection systems. Although exhaustive for its time the work reported was limited to 2-D airfoils and simple

3-D geometries. Empirical relations were defined in order to allow the results to be extended to realistic 3-D geometries used on design aircraft while being subject to the known limitations of empirical extrapolation. An execution of a battery of experiments covering all geometries and operational conditions of relevance to aircraft icing would have been cost prohibitive and complicated (if not impossible) to achieve, due to the wide range of aircraft types to be covered whether performed in wind tunnels or in actual flight missions.

The apparition of computers in the 1970's allowed icing scientists to tackle the problem from a computational perspective. Different 1-D and 2-D codes appeared in the U.S.A. and Europe using mostly similar techniques in order to solve for water impingement and ice accretion. The best known codes using these approaches are NASA's Lewice[2] and the ONERA's icing code[3]. These codes originally used panel methods to compute the inviscid air velocity on the geometry surface. The surface velocity solution was then coupled with boundary layer codes or integral codes to obtain the viscous velocity field around the geometry. These codes had several drawbacks when it came to calculate impingement coefficients. Some of these drawbacks are:

- The droplets impingement coefficients are calculated by launching particles upstream in the flowfield and painstakingly calculating their trajectories using Lagrangian particle-tracking techniques;
- Uncertainties arise as to where to inject the particles and how many particles to use to accurately predict impingement regions, the latter question being limited by computational resources;
- Some parts of highly complex geometries such as recirculating regions of multi-element airfoils are very difficult to attain and it is never evident where to launch particles in order to impinge on these regions, hence a further trial and error;
- 2-D cases might be possible to analyze in reasonable times and with acceptable computational requirements but uncertainty will always arise about regions of complex

2-D and 3-D geometries where impingement was not observed unless verified by experiments.

Further evolutions of these Lagrangian codes were based on Navier-Stokes aerodynamic solvers as Computational Fluid Dynamics evolved but little was done to overcome the limitations of Lagrangian particle tracking in 3-D mode.

Recent advances in the development of icing simulation codes at the Concordia university CFD Lab make it affordable to realistically simulate 3-D water droplets impingement in icing situations, for complex 3-D geometries in real icing environmental conditions as provided by icing atmospheric databases. The present thesis is a first application of these developments and looks at the feasibility of applying such modern icing simulation technologies to analyze in-flight icing susceptibility to meteorological conditions. The air flow is determined using a finite element solution of the Navier-Stokes equations, providing a more complete solution for the air flow on the surface and around the geometry. A system of partial differential equations is proposed in order to represent the droplets flow with the possibility of adding or removing as many terms as needed in order to better model the physics of icing[4]. This approach is a fully 3-D one where droplets velocity and volume fraction of water have to be computed only at the nodes where the air flow variables are determined, dispensing with particles having to be tracked as they cross the mesh as with Lagrangian tracking approaches.

On the experimental side, Environment Canada's (EC) Atmospheric Environment Services (AES) has conducted a number of in-flight data acquisition experiments, and in particular the Canadian Freezing Drizzle Experiment (CFDE)[5, 6, 7, 8]. The CFDE consists of collecting SCWD impingement data around various locations of a Convair-580 aircraft flying in icing clouds and has been in the winter of 1997 in its third phase, the CFDE III. The AES staff also had concerns whether significant water droplets impingement and ice formation can be expected at the windows of the test aircraft and in particular the side window which is not heated. The CFD lab was required to conduct a numerical study of water

droplets impingement on the nose/cockpit geometry of the Convair-580 with specific water droplets diameters. The droplets impingement and surface water collection efficiency around the nose and cockpit profile of the Convair-580 aircraft are computed numerically using the Eulerian scheme. Following a description of the scheme and validation of the code using existing 3-D experimental impingement data, results on that geometry will be presented and discussed in this thesis. These results will help the AES team improve their data acquisition techniques and possibly point out potential impingement areas around the aircraft's windows.

Chapter 2

Physical Model

This chapter will introduce the physical model which is used in order to describe the motion of a droplet phase in an air flow through a multiphase flow approach. The relative properties of a component i in a multiphase flow are defined by its volume fraction α_i and its bulk density ρ_{bi} . The volume fraction of a component (water droplets phase, for example) is

$$\alpha_i = v_i/V_{mix}$$

where v_i is the volume of component i in the mixture and V_{mix} the volume of the mixture. The sum of volume fractions of all components in a multiphase flow adds up to unity. The component bulk density is

$$\rho_{bi} = m_i/V_{mix}$$

where m_i is the mass of component i in the mixture. The sum of bulk densities of all components adds up to the density of the mixture. The ratio of the mass of each component to the mass of the conveying phase is the component loading.

In icing conditions the loading of water with respect to air is of the order of 10^{-3} . For loadings smaller than 0.1, the flow is considered dilute and the presence of the particles does not affect the properties of the conveying phase, ie. the air flow. Thus the air flow

is solely responsible for particle transport and particle property changes. This condition is best modeled by one-way coupling[11, page 299] where an air flow solution is obtained first and used to calculate a corresponding droplet solution. The following assumptions can then be made:

- 1) The droplets are spherical without any deformation or breaking;
- 2) no droplets collisions or coalescence;
- 3) no droplets splashing at the walls;
- 4) no heat and mass exchange between the droplets and the air phases;
- 5) turbulence effects on the droplets flow are neglected;
- 6) the only forces acting on the droplets are due to air drag, gravity and buoyancy.

The first three assumptions rely on the fact that icing flows are dilute, with volume fractions of the order of 10^{-6} , and that droplets are small with MVD in the range of 1-1000 microns. The fourth assumption is justified as only impingement is required at this stage of the work. Heat exchange between the two phases is important once ice accretion is required. The fifth assumption relies on the fact that turbulence effects are addressed on the aerodynamic side while computing the aerodynamic solution. Moreover, it is not the goal of this thesis to investigate turbulence effects on droplet flow but to study the applicability of Eulerian methods to 3-D droplet impingement with special emphasis on side-window impingement.

The droplets flow one-way coupling model consists of a continuity equation and a momentum equation which are respectively written in non-dimensional form as[9]:

$$\frac{\partial \alpha}{\partial t} + \nabla \cdot (\alpha \mathbf{u}) = 0, \quad (2.1)$$

$$\frac{\partial \mathbf{u}}{\partial t} + \mathbf{u} \cdot \nabla \mathbf{u} = \frac{C_D Re_d}{24K} (\mathbf{u}_a - \mathbf{u}) + \left(1 - \frac{\rho_a}{\rho}\right) \frac{1}{Fr^2} \mathbf{g} \quad (2.2)$$

where the variables $\alpha(x, t)$ and $\mathbf{u}(x, t)$ are mean values, respectively, of the water volume fraction and of the droplets velocity over the element, given a small fluid element around any specific location x in space, at time t .

\mathbf{u}_a = non-dimensional velocity of air,

ρ = density of water,

ρ_a = density of air,

d = droplets diameter,

$Re_d = \rho d U_\infty |\mathbf{u}_a - \mathbf{u}| / \mu$ is the droplets Reynolds number,

$K = \rho d^2 U_\infty / 18 L \mu$ is an inertia parameter,

$C_D = (24/Re_d)(1 + 0.15 Re_d^{0.687})$ for $Re_d \leq 1000$ is an empirical drag coefficient for spherical droplets [10],

$Fr = U_\infty / \sqrt{L g_0}$ is the Froude number.

The first term on the right-hand-side of equation (2.2) represents the air drag force on the droplets, while the second term represents the buoyancy and gravity forces.

A parameter of great interest in icing, the water collection efficiency, can also be readily solved for using the obtained values of volume fraction and droplets velocity. The water collection efficiency at the surface, or normalized flux of water at the surface with respect to the water flux at infinity, determines the amount of water flowing on the surface, which subsequently determines the amount of ice formation and de-icing requirements. In the Eulerian context, the water collection efficiency is calculated at every surface point using

$$\beta = -\alpha \mathbf{u} \cdot \mathbf{n}$$

where \mathbf{n} is the surface normal. Special care has to be given to evaluating the surface normals in 3-D. If we consider a node on an element face i on a surface, the surface normal n_i at this node is

$$n_i = v_1 \times v_2$$

where n_i is the counter-clockwise vector product of v_1 and v_2 , the two vectors along face edges originating from the node in question. The counter-clockwise rotation ensures a normal vector direction exiting from the surface. In order to account for surface discretization we would need to average n_i over all the surface faces of all the elements connected to that particular node, giving,

$$n = \sum_e n_i$$

The water flux at the surface can then be calculated as

$$m_w = \text{LWC } U_\infty \beta \quad (2.3)$$

The system of equations (2.1)–(2.2) is similar to a compressible Euler system without the pressure term. There is no equation of state either for the droplets phase. These absences denote one of the main differences between a continuum such as a gas phase and a dilute particle cloud such as a water droplets cloud in icing conditions. In a continuum, information is transmitted by pressure waves and property diffusivity such as viscosity and thermal conductivity. In a particle cloud, there is no analog to pressure and information is transmitted along particle trajectories rather than through particle collisions. Property diffusion of the particle phase would be mainly due to the conveying phase turbulence effects which are not well understood at the moment.

The system (2.1)–(2.2) models only one droplet size at a time. This size can be chosen to be the MVD of the droplets cloud. In order to simulate variable droplets size or droplets size distributions, the system (2.1)–(2.2) would have to be solved for each individual droplet size and the different solutions combined using the percentage of each size in the distribution. For example, the calculation of overall water collection efficiency for a flow with a given droplets size distribution is done by using

$$\beta = \sum_i p_i \beta_i$$

where β_i and p_i are, respectively, the collection efficiency and the percentage of droplets of the i^{th} -class within the droplets size distribution.

Obviously, the Eulerian approach allows us to include as much physics to the approach as eventually needed since it would merely consist of adding or removing terms to the

system (2.1)–(2.2). The volume fraction, velocity and collection efficiency of the droplets phase are also readily solved for in an integrated manner and available anywhere in the flow field. The heat transfer coefficients are obtainable from the air flow solution where they were solved for simultaneously with the other air flow parameters. This is not the case for the Lagrangian approach where post-treatment is needed to obtain collection efficiency. There is also no guarantee that droplets parameters at all points in the flow will be available since the Lagrangian technique consists mainly of releasing particles in the flow field and "hoping" that they will impinge on desired locations, much in a shoot-out fashion. Areas with recirculating flows such as inter-element gaps for multi-element airfoils can be completely missed with little hope of attaining them.

Chapter 3

Computational Approach

3.1 Air Flow Code

The air flow solution is computed prior to the droplets solution using the resident CFD Lab air flow code Finite Element Navier-Stokes Analysis Package (FENSAP). FENSAP was originally written at the CFD Lab and is continuously under development by the lab's staff[12, 13]. The code has the ability to analyze steady or unsteady compressible turbulent flows, with or without recirculations, and can provide an inviscid flow simulation by default should this simplification prove justifiable in adequate situations. FENSAP is essentially a 3-D code but is capable of analyzing 2-D flows as well. The following algorithmic developments are included in FENSAP:

- Structured and unstructured grids using hexahedral/tetrahedral/prismatic finite elements over complex geometries typical of industrial applications;
- Weak-Galerkin and Least-Squares formulations;
- Implicit time-stepping methods combined with efficient iterative solvers and preconditioners with optimized memory requirements;
- Shared-memory parallelization of large portions of the code;

- $\kappa - \epsilon$ high-Reynolds number turbulence model with logarithmic finite elements at the wall, considerably reducing the size of grids for turbulent flows;
- Low-Reynolds number turbulence model to examine the effect of sand-paper roughness on near-wall physics;
- Arbitrary Lagrangian-Eulerian (ALE) formulation for problems with changing boundaries, such as ice growth on an airfoil;
- Full compatibility with an efficient anisotropic Mesh Optimization Methodology (MOM) package, also developed at the CFD Lab, that has been shown to give highly accurate user-, solver- and initial mesh-independent results[14].

3.2 Droplets Flow Code

3.2.1 Algorithmic Features

The droplet code, written by Professor Bourgault, is finite element-based with the possibility of using either a viscous or an inviscid air flow solution for droplet calculations. The following algorithmic developments are included in the droplets code:

- 2-D and 3-D meshes capability with hexahedral/tetrahedral/prismatic finite elements;
- Streamline Upwinding Petrov-Galerkin (SUPG) terms added[15] to prevent oscillations in the solution, with discontinuity capturing crosswind terms[16] to stabilize droplet solutions with contact discontinuities;
- A non-linear Newton-GMRES algorithm[17] is used to solve the nonlinear system of equations. This solver combined with diagonal preconditioning requires very little memory since it does not store the system matrix and is a compromise, efficiency wise, between an explicit and a fully implicit solver with ILU preconditioning;

- Parallelization of the element assembly calculation routines through an element coloring scheme[18].

3.2.2 Discretization

The discretization of the system of equations (2.1)–(2.2) is carried out through a finite element Galerkin formulation. Considering a domain Ω of continuous piecewise linear elements for tetrahedra (quasi-linear for hexahedra), the volume fraction α^n and the droplets velocity \mathbf{u}^n at time t^n are solutions of

$$\begin{aligned} \int_{\Omega} \left[\frac{\alpha^n - \alpha^{n-1}}{k} + \nabla \cdot (\alpha^n \mathbf{u}^n) \right] \varphi \, dx \\ + a_{\alpha}(\alpha^n, \varphi) + a_{\parallel \alpha}(\alpha^n, d\varphi) = 0 \end{aligned} \quad (3.1)$$

$$\begin{aligned} \int_{\Omega} \left[\frac{\mathbf{u}^n - \mathbf{u}^{n-1}}{k} + \mathbf{u}^n \cdot \nabla \mathbf{u}^n \right] \cdot \psi \, dx \\ + a_{\mathbf{u}}(\mathbf{u}^n, \psi) + a_{\parallel \mathbf{u}}(\mathbf{u}^n, d\psi) = \int_{\Omega} \mathbf{f} \cdot \psi \, dx \end{aligned} \quad (3.2)$$

for all $\varphi \in V_h, \psi \in V_h^N$. N is the number of spatial dimensions. \mathbf{f} is equivalent to the drag, buoyancy and gravity force terms on the right hand side of equation (2.2) and depends on \mathbf{u} and \mathbf{u}_a . The terms $a_{\alpha}(\cdot, \cdot)$ and $a_{\mathbf{u}}(\cdot, \cdot)$ are the SUPG stabilization terms expressed as

$$a_{\alpha}(\alpha, \varphi) = c_{\alpha} \sum_K \int_K \left[\frac{\alpha^n - \alpha^{n-1}}{k} + \nabla \cdot (\alpha^n \mathbf{u}^n) \right] \tau_K (\mathbf{u}^n \cdot \nabla) \varphi \, dx \quad (3.3)$$

$$a_{\mathbf{u}}(\mathbf{u}^n, \psi) = c_{\mathbf{u}} \sum_K \int_K \left[\frac{\mathbf{u}^n - \mathbf{u}^{n-1}}{k} + \mathbf{u}^n \cdot \nabla \mathbf{u}^n - \mathbf{f} \right] \tau_K (\mathbf{u}^n \cdot \nabla) \psi \, dx \quad (3.4)$$

where c_α and c_u are user-provided parameters. τ_K is equal to $h_K/\sqrt{1+|u|^2}$, h_K being the specific size of element K . The terms $a_{||\alpha}(\cdot, \cdot)$ and $a_{||u}(\cdot, \cdot)$ are the discontinuity capturing cross-wind diffusion terms and are expressed as

$$a_{||\alpha}(\alpha^n, d\varphi) = c_{||\alpha} \sum_K \int_K \left[\frac{\alpha^n - \alpha^{n-1}}{k} + \nabla \cdot (\alpha^n \mathbf{u}^n) \right] \tau_K(\mathbf{u}_{||\alpha}^n \cdot \nabla) \varphi dx \quad (3.5)$$

$$a_{||u}(\mathbf{u}^n, d\psi) = c_{||u} \sum_K \int_K \left[\frac{\mathbf{u}^n - \mathbf{u}^{n-1}}{k} + \mathbf{u}^n \cdot \nabla \mathbf{u}^n - \mathbf{f} \right] \tau_K(\mathbf{u}_{||u}^n \cdot \nabla) \psi dx \quad (3.6)$$

where $c_{||\alpha}$ and $c_{||u}$ are user-specified parameters as multiples of c_α and c_u respectively. $\mathbf{u}_{||\alpha}^n$ and $\mathbf{u}_{||u}^n$ are calculated using the expression

$$\mathbf{u}_{||x}^n = \begin{cases} \frac{(\mathbf{u} \cdot \nabla x^h)}{|\nabla x^h|_2^2} \nabla x^h & \text{if } \nabla x^h \neq 0 \\ 0 & \text{if } \nabla x^h = 0 \end{cases} \quad (3.7)$$

3.2.3 Boundary Conditions

The system of equations (2.1)–(2.2) has been shown to be hyperbolic [4]. A boundary condition needs then to be imposed on every inlet boundary for every variable. No boundary conditions are needed on the walls or on the outlet boundaries. The initial solution is specified as $\alpha = 1$ and $\mathbf{u} = \mathbf{u}_\infty$ everywhere in the flowfield except at the walls where these values are set to zero. \mathbf{u}_∞ is typically the flow velocity at infinity but, can also be the sum of the flow velocity and the droplets free-fall terminal velocity in order to account for droplets initial velocity in the cloud.

Chapter 4

CAD Modeling and Meshing Techniques

All CAD models for test-cases and the Convair-580 aircraft nose/cockpit geometry were constructed using ICEM CFD's CAD module DDN. The input data for the Convair was supplied by AES from hardcopy blueprint measurements as a CAD version was not available. All the data was in xyz point format as shown in Figure 4.1.

The point input data was used to produce B-spline curves describing the geometry using DDN. In the 3-D cases, B-spline surfaces were also generated to fully describe the geometries. The geometries were then enclosed by solution domains, 2-D elliptic sections for 2-D cases and 3-D ellipsoid sections for 3-D cases. Figure 4.2 shows the resulting Convair-580 geometry from data taken from files such as in Figure 4.1, fitted into a quarter

```
\ Post Geometry.  
  x      y      z  
.000  74.310  26.010  
.000  74.610  26.980  
.000  74.890  27.940  
.000  75.230  29.160  
.000  75.550  30.350  
.000  75.830  31.480  
.000  76.130  32.710  
.000  76.400  33.960  
.000  76.650  35.130  
.000  76.920  36.520  
.000  77.190  37.970  
.000  77.420  39.300  
.000  77.630  40.290
```

Figure 4.1: Example of an input data file for the Convair-580 geometry

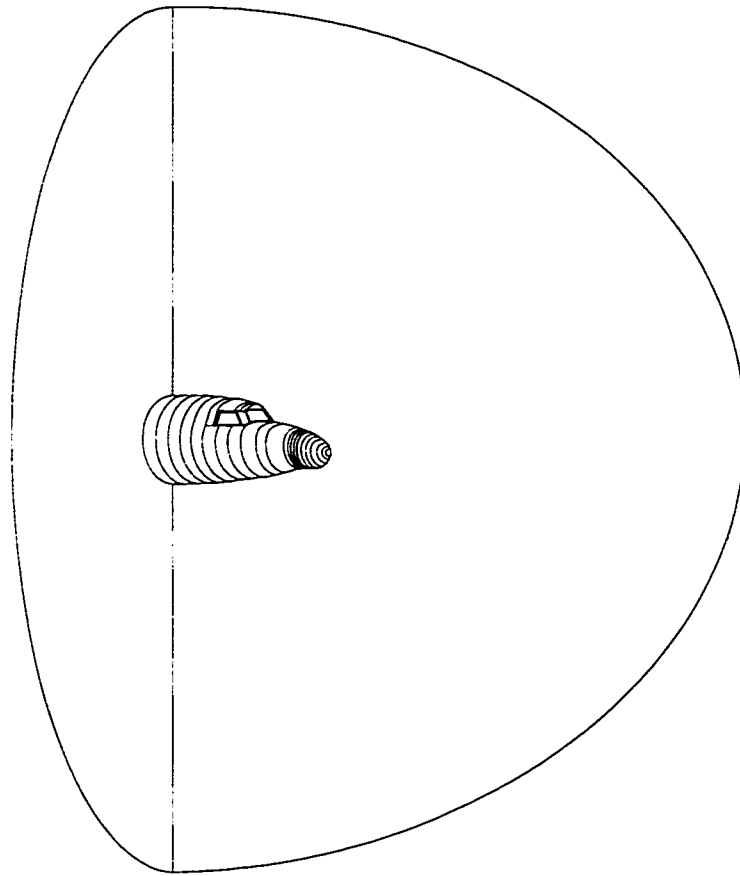


Figure 4.2: Convair-580 nose/cockpit geometry with its quarter-ellipsoid solution domain of an ellipsoid solution domain.

The resulting CAD models and domains were then divided into blocks using ICEM CFD's hexahedral meshing model HEXA. The blocking makes it easier to control different local meshing requirements for the geometries. Structured C-grids with linear 8-nodes hexahedral elements were exclusively used for all geometries. Figures 4.3 and 4.4 show the Convair-580 blocking and one of the resulting Convair structured hexahedral meshes respectively. Figure 4.5 shows the same Convair mesh at the body surface of the aircraft.

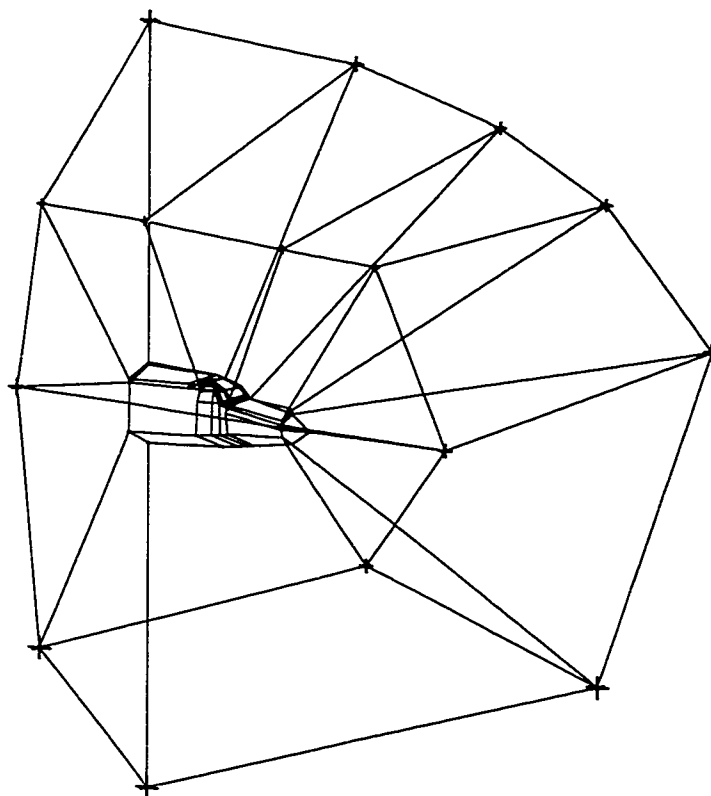


Figure 4.3: Convair-580 nose/cockpit blocking

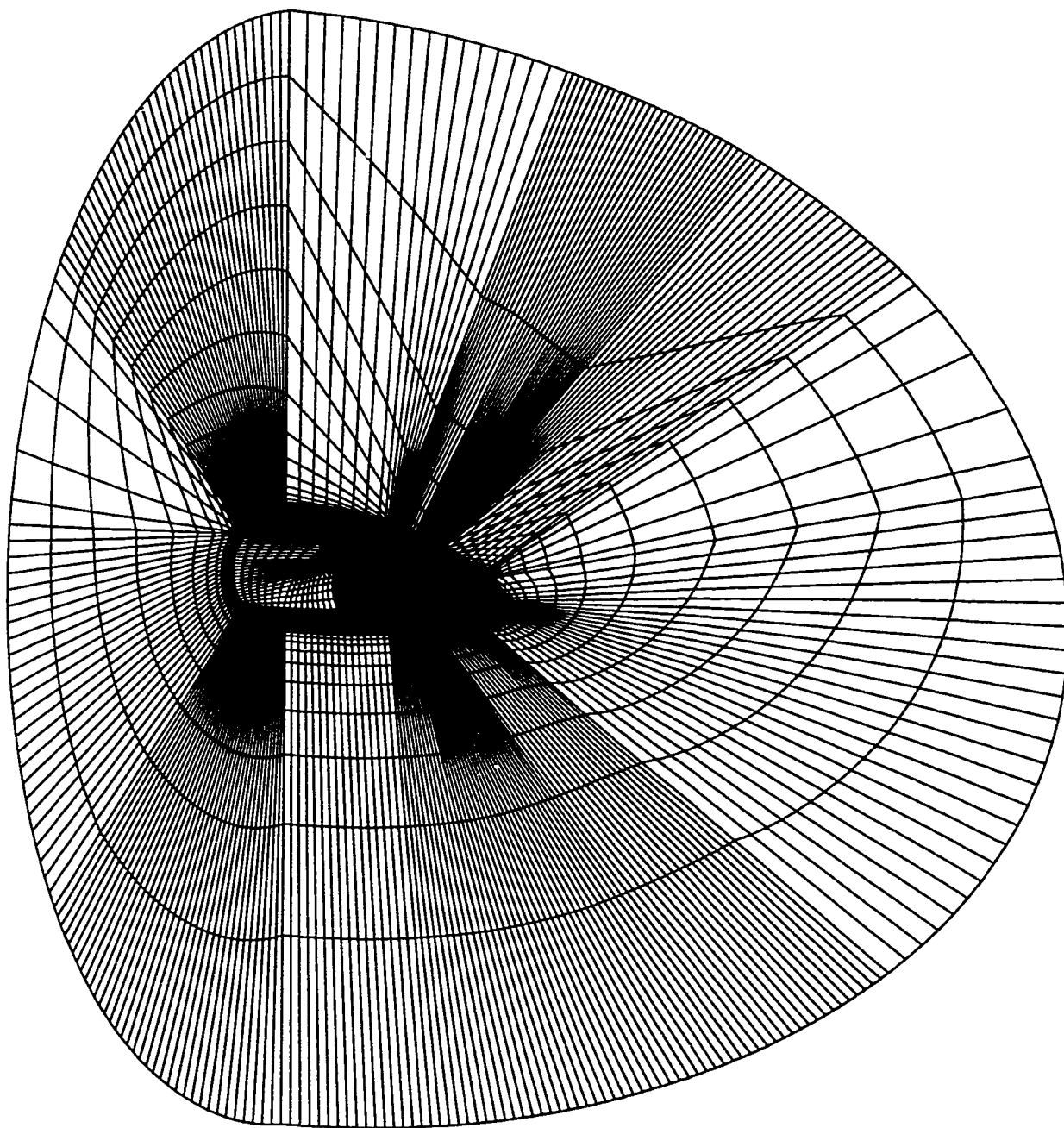


Figure 4.4: Convair-580 nose/cockpit Euler air flow solution structured mesh with 156095 nodes and hexahedral elements

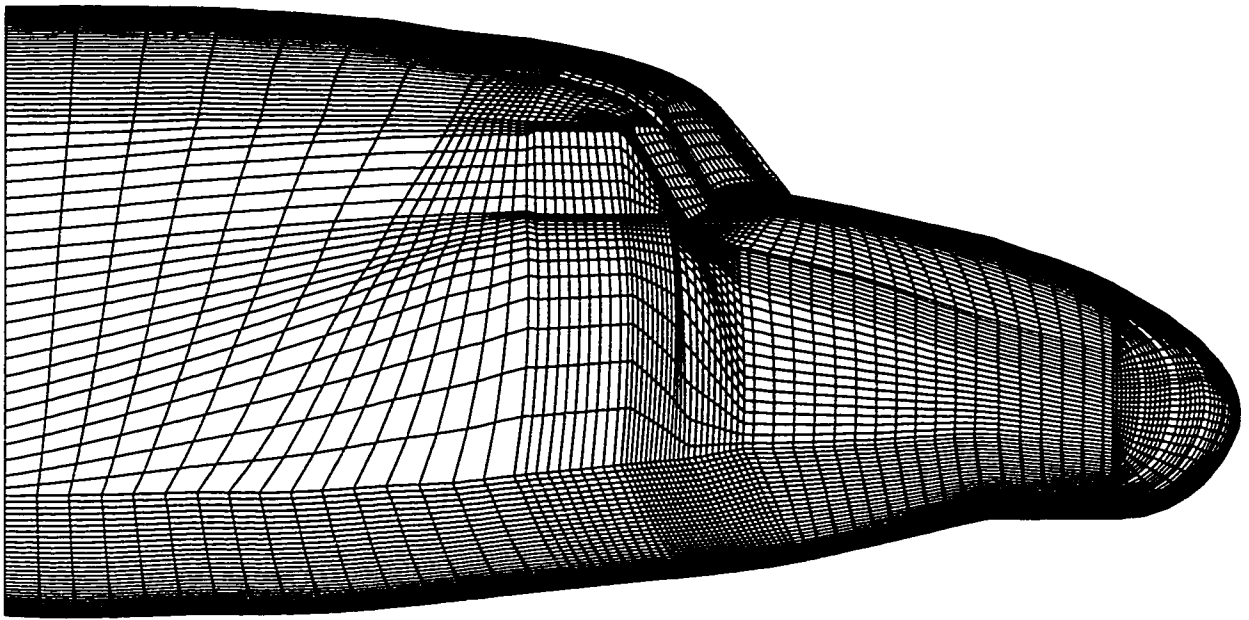


Figure 4.5: Convair-580 nose/cockpit Euler air flow solution structured mesh on the aircraft body surface

Chapter 5

Droplet Code Validation and Test Cases

The droplet code was validated with 2-D and 3-D experimental results [19] consisting of experimental impingement limits and surface collection efficiency measurements on the surface of a 2-D cylinder and a 3-D sphere, respectively. Inviscid air flow solutions were used for both cases. The geometries were constructed using ICEM CFD's DDN module. The meshes were constructed using ICEM CFD's hexahedral meshing module HEXA.

5.1 2-D Test Case

The 2-D cylinder test case consisted of a structured O-grid hexahedral mesh around a cylinder with a diameter of 10.16 cm. The mesh is shown in figure 5.1 and the pressure field of the inviscid airflow solution calculated on it in figure 5.2. The structured 2-D mesh has 17168 nodes. The physical parameters for the airflow and droplets solution are the following:

$U_{\infty} = 80m/s$, the air flow velocity at infinity;

$\rho_{a\infty} = 1.097kg/m^3$, the air flow density at infinity;

$M_{\infty} = 0.236$, the Mach number at infinity;

$T_{\infty} = 12^{\circ}K$, the static temperature at infinity;

$P_{\infty} = 89867Pa$, the static pressure at infinity.

Droplets solutions were calculated for the 2-D cylinder geometry for each of the droplets diameters in Table 5.1 which all together form a Langmuir-D distribution with an MVD of $16\mu m$. Figure 5.3 shows the collection efficiency on the cylinder surface for one droplet diameter of $16\mu m$. Figure 5.4 shows the collection efficiency for the combined result of the solutions for all the diameters in the distribution. Not much difference can be seen at first look. However, should one plot the collection efficiency on the surface for both cases and compare to experimental results [2], important differences come to light. Such a plot is shown in figure 5.5 and it can clearly be seen that the Langmuir distribution is much more effective than the MVD solution in matching the experimental data. The Langmuir solution captures both maximum collection efficiency and impingement limits values and stays within the experimental repeatability range. The MVD solution on the other hand overestimates the maximum impingement value, underestimates the impingement limits and goes out of the experimental repeatability range in some areas. We can conclude from our results that FENSAP-ICE is capable of providing quality 2-D droplets impingement data, given an adequate droplets distribution is provided to represent the actual droplets flow field.

5.2 3-D Test Case

The sphere test case's mesh consists of an C-grid around the surface of a $15.04cm$ diameter half-sphere. The sphere's hexahedral mesh consists of 201735 nodes forming 185976 linear hexahedral elements in a half spherical domain. Figure 5.6 shows the hexahedral mesh and solution domain for the sphere test case. Figure 5.7 shows a closeup of a cut perpendicular to the x-axis through the center of the sphere. The direction of the air flow is along the z-axis from $-\infty$ to $+\infty$.

The inviscid air flow solution input parameters were:

Table 5.1: Langmuir-D distribution of droplet diameters with an MVD of $16\mu\text{m}$ as used for the 2-D cylinder testcase

Percentage LWC	Ratio of Diameters	Droplet Diameter (μm)
5	0.31	5.0
10	0.52	8.3
20	0.71	11.4
30	1.00	16.0
20	1.37	21.9
10	1.74	27.8
5	2.22	35.5

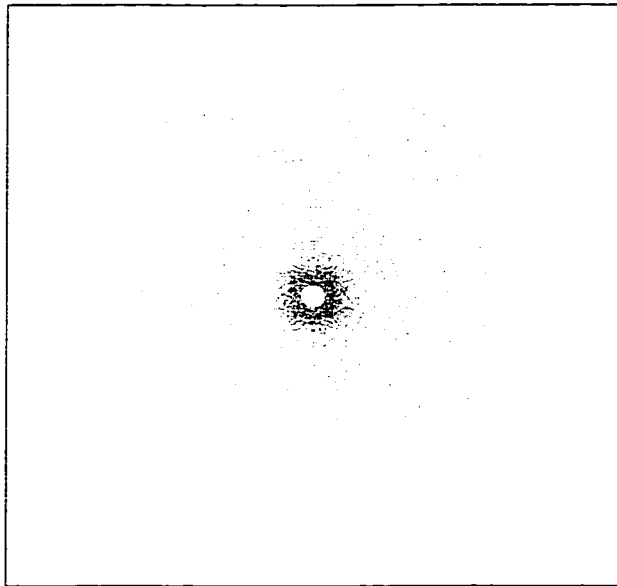


Figure 5.1: Side view of the 2-D cylinder validation mesh

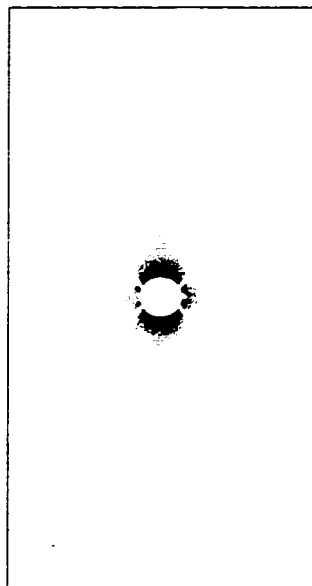


Figure 5.2: Inviscid pressure field around the 2-D cylinder geometry

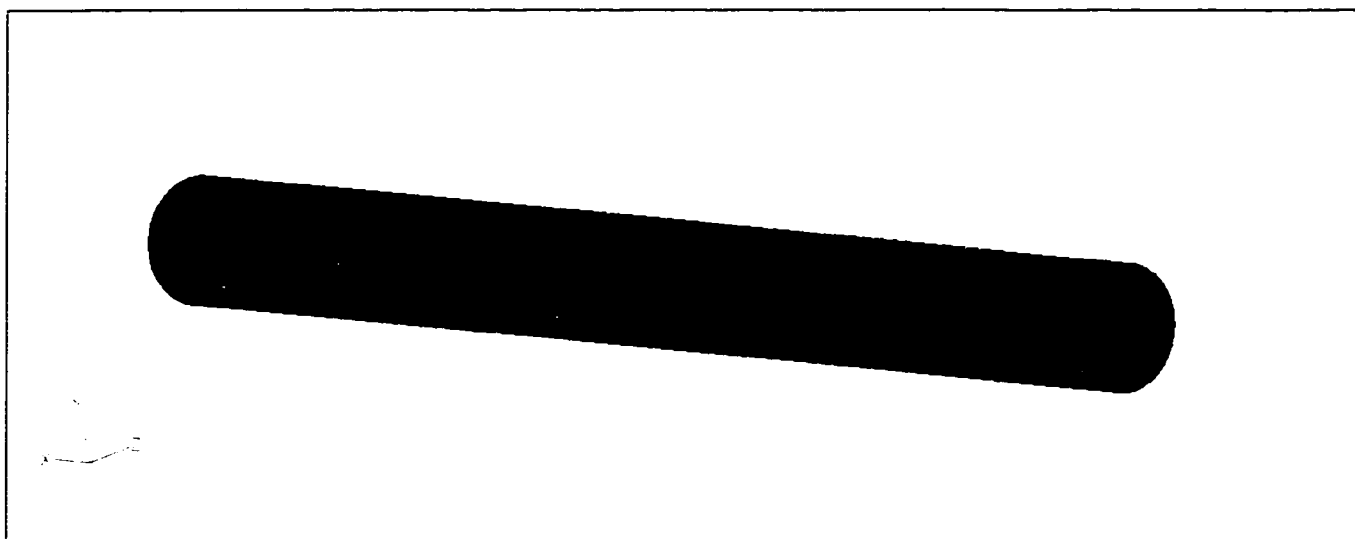


Figure 5.3: Collection efficiency at the surface of a 2-D cylinder for a droplet diameter of $16\mu\text{m}$

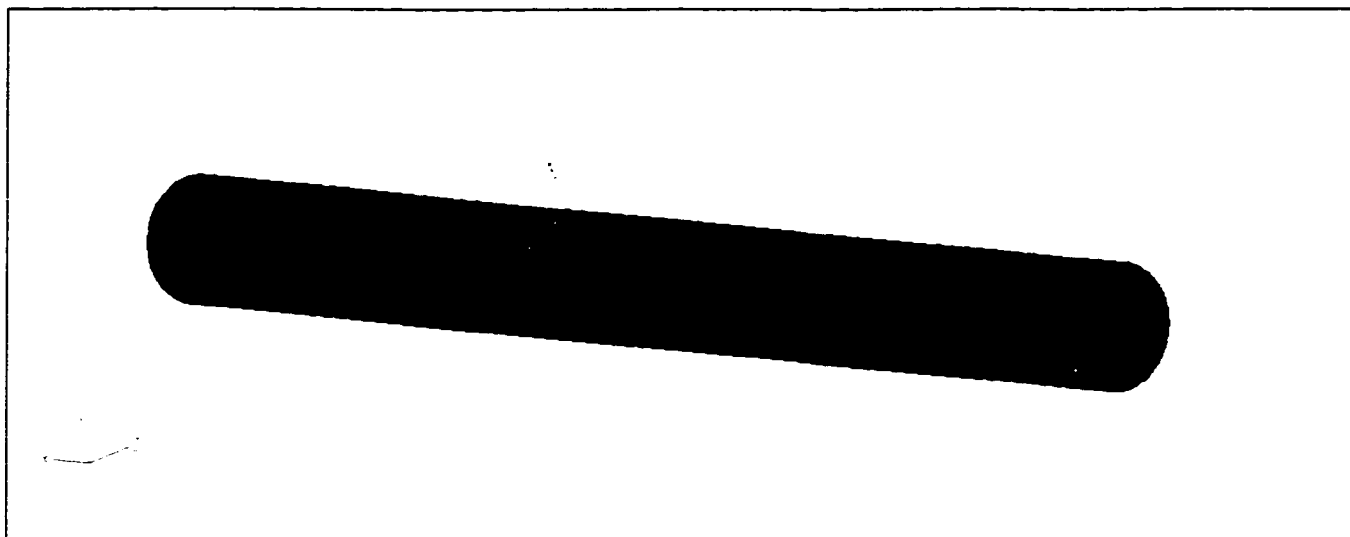


Figure 5.4: Collection efficiency at the surface of a 2-D cylinder for a Langmuir-D distribution with an $MVD = 16\mu\text{m}$

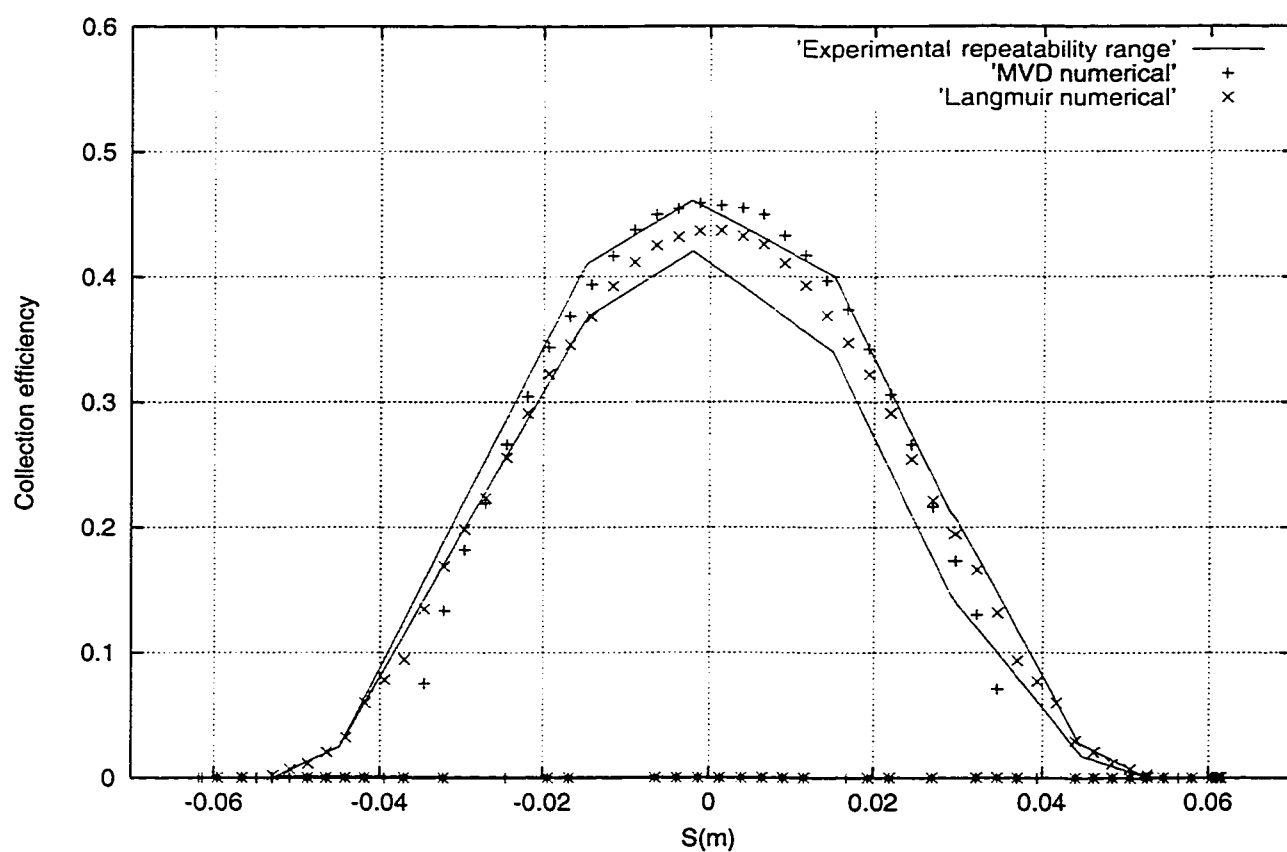


Figure 5.5: Comparison of computed collection efficiency on the surface of the 2-D cylinder for the Langmuir distribution and the MVD solution to experimental data

$U_{\infty} = 75m/s$, the air flow velocity at infinity;

$\rho_{a\infty} = 1.097kg/m^3$, the air flow density at infinity;

$M_{\infty} = 0.217$, the air flow Mach number at infinity;

$T = 7^{\circ}C$, the static temperature;

$P = 95840Pa$, the static pressure.

Figure 5.8 shows the pressure field for the inviscid air flow solution around the sphere.

No comparison could be made between our numerical data and experimental data since experimental surface measurements of aerodynamic parameters were not provided in the literature.

Droplet solutions were computed for the seven droplet diameters shown in Table 5.2. These droplet diameters form a Langmuir-D distribution with an MVD = $18.6\mu m$. The surface collection efficiencies are shown in figures 5.9, 5.10, 5.11, and 5.12 for droplet diameters of 5.8 and 9.7, 13.2 and 18.6, 25.5 and 32.4, and $41.3\mu m$, respectively. The combined solution obtained using the method described in chapter 2 is shown in figure 5.13 side by side and on the same collection efficiency scale as the MVD = $18.6\mu m$ solution. Since all the figures are drawn to the same scale it can be seen that the maximum collection efficiency, as well as the impingement limits, increase steadily as the droplet diameter increases. Moreover, the MVD = $18.6\mu m$ solution seems to result in a higher maximum collection efficiency than the Langmuir distribution combined solution, judging from the higher concentration of red at the center of the sphere which is a sign of increased collection. For a quantitative evaluation one has to look at figure 5.14 which shows a plot of the surface collection efficiency vs distance from the stagnation point for the combined solution, the MVD = $18.6\mu m$ solution and the experimental results [19]. The MVD = $18.6\mu m$ collection efficiency curve slightly overestimates the maximum experimental collection efficiency and underestimates the experimental limits of impingement. However,

most of the MVD collection efficiency curve falls within the reported experimental margins of error of $\pm 10\%$. The combined solution on the other hand matches the experimental maximum collection efficiency as well as the maximum impingement limits. The rest of the combined solution curve falls within the experimental margins of error as well. Both solutions on the other hand are slightly out of the experimental margins of error in the region just before the maximum impingement limits. With respect to the MVD solution this clearly demonstrates its unsuitability to simulate an experimental water droplets flow. The combined solution, however, showed itself to be more suitable for this purpose but the differences from experimental results near the maximum impingement limits region make one wonder if the Langmuir distribution chosen in the literature [19] to approximate the droplets flow is really representative. A more accurate measured distribution would have been desirable. We should also mention the following points about the experimental data:

- The experimental range of repeatability reported was an average over the whole range of measurements and not a local range as for the cylinder data. A more accurate estimate of the experimental range of repeatability would be desirable for better comparison to numerical results;
- The experimental data dates back to the mid-50's and recent studies pointed to uncertainties in the data measurement techniques [20] resulting in over- and under-estimation at different points within the same set.

These remarks increase the level of confidence in FENSAP-ICE. Overall, one can say that FENSAP-ICE is capable of providing quality results in 3-D, given the adequate droplets and flow experimental conditions.

Table 5.2: Langmuir-D distribution of droplet diameters with an MVD of $18.6\mu\text{m}$ as used for the 3-D sphere test-case

Percentage LWC	Ratio of Diameters	Droplet Diameter (μm)
5	0.31	5.8
10	0.52	9.7
20	0.71	13.2
30	1.00	18.6
20	1.37	25.5
10	1.74	32.4
5	2.22	41.3

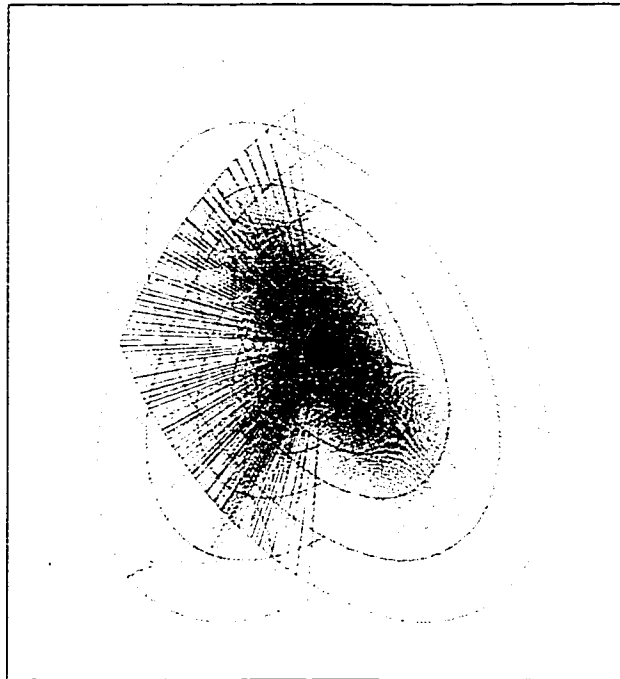


Figure 5.6: Hexahedral mesh for the sphere test-cases

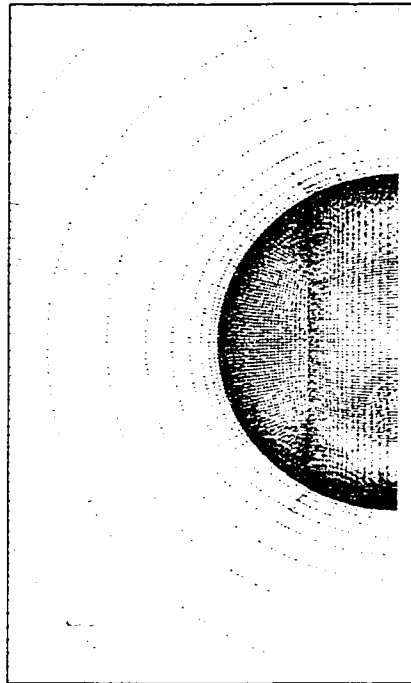


Figure 5.7: Closeup of a cut through the center of the sphere

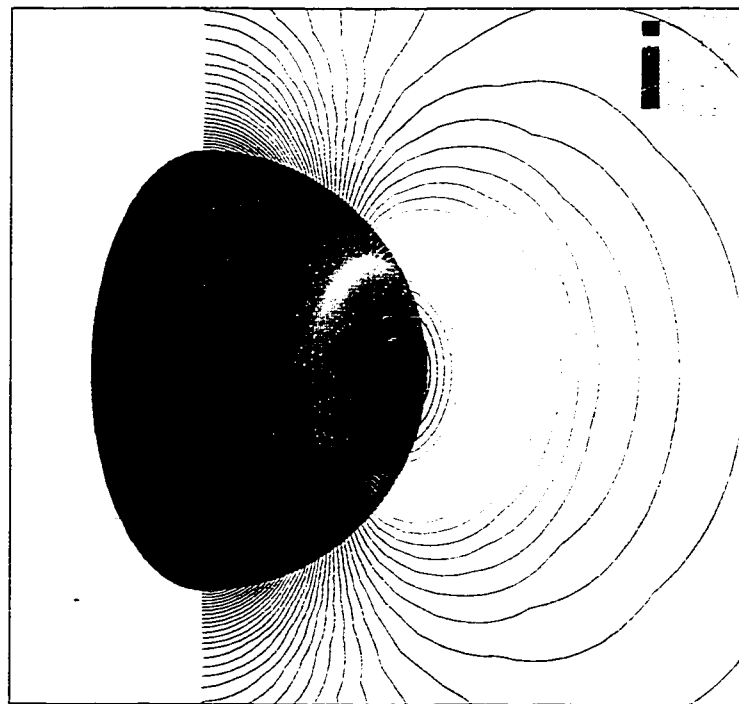


Figure 5.8: 15.04cm Sphere inviscid solution pressure field

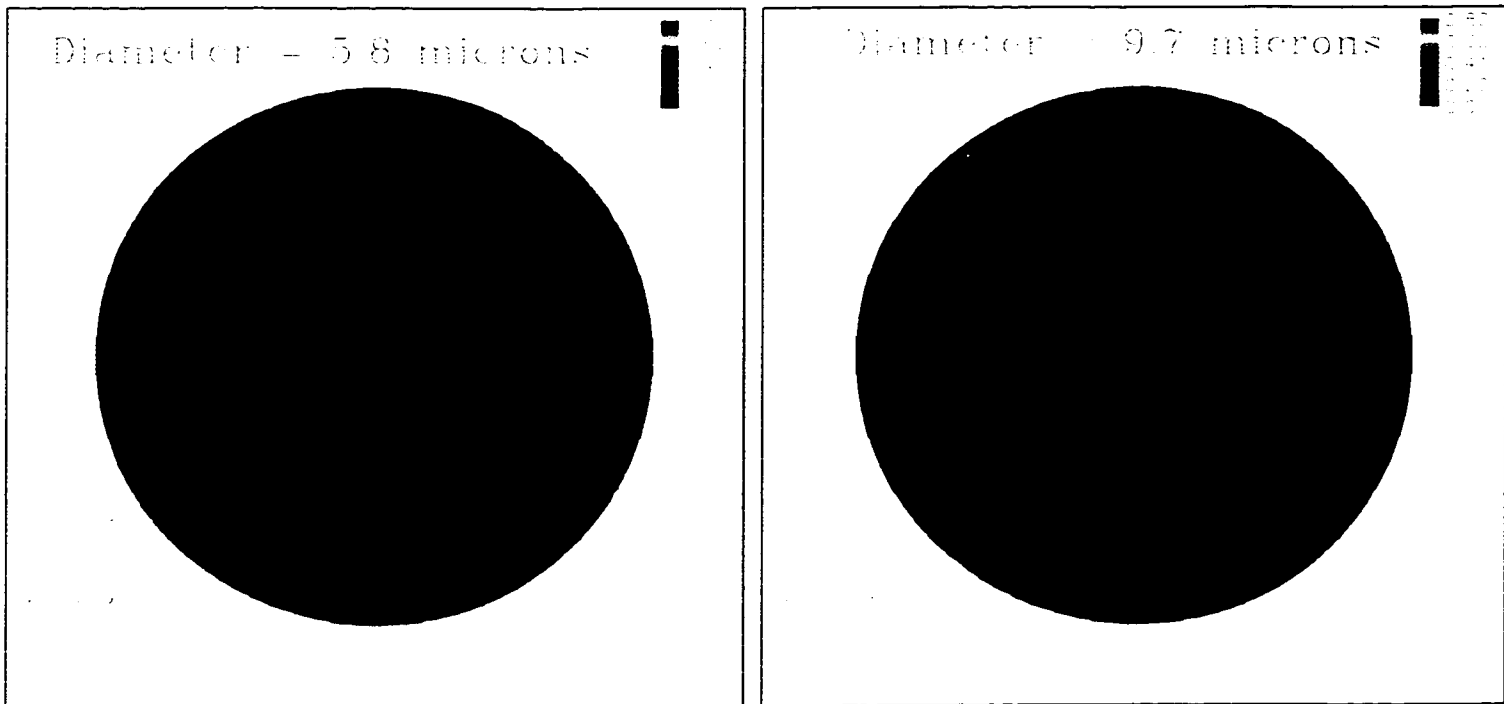


Figure 5.9: 15.04cm sphere surface collection efficiency for $d=5.8\mu m$ (left) and $d=9.7\mu m$ (right)

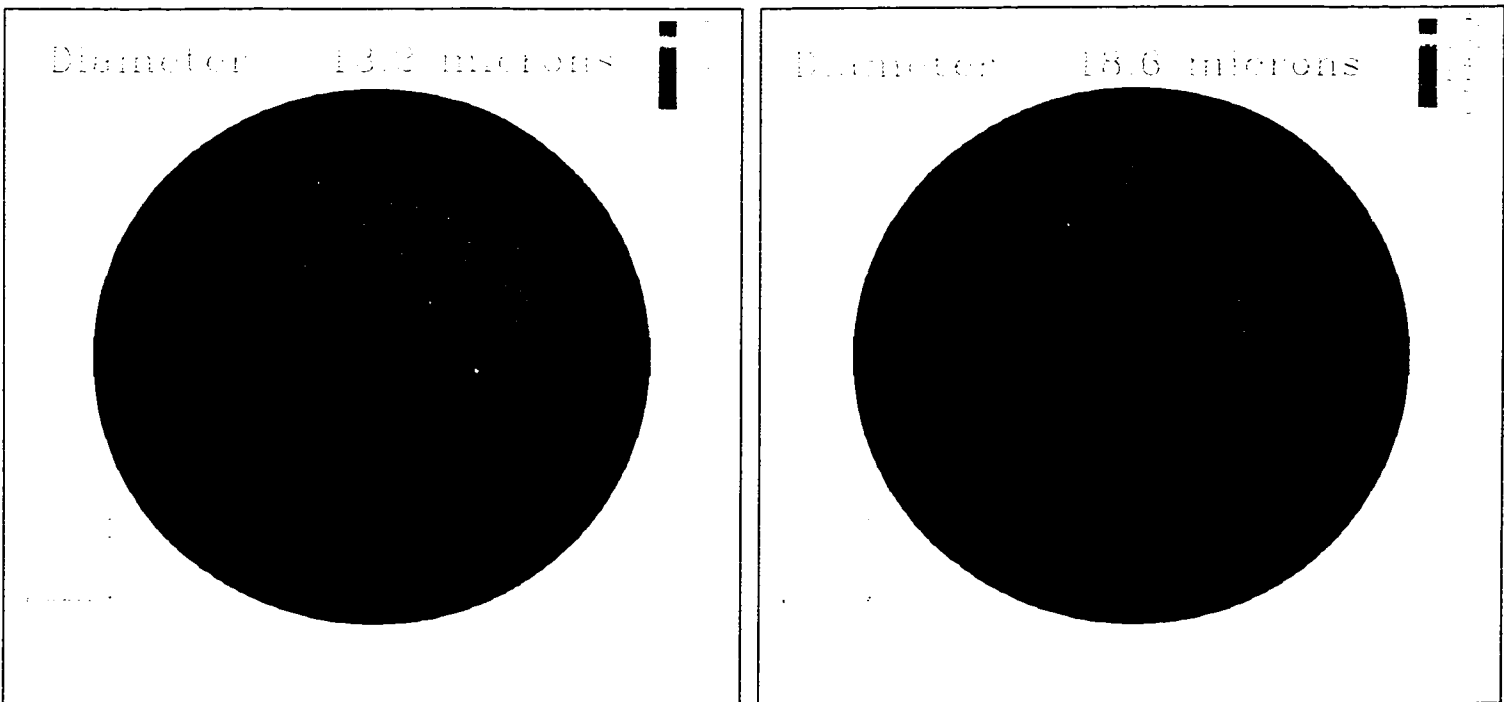


Figure 5.10: 15.04cm sphere surface collection efficiency for $d=13.2\mu m$ (left) and $d=18.6\mu m$ (right)

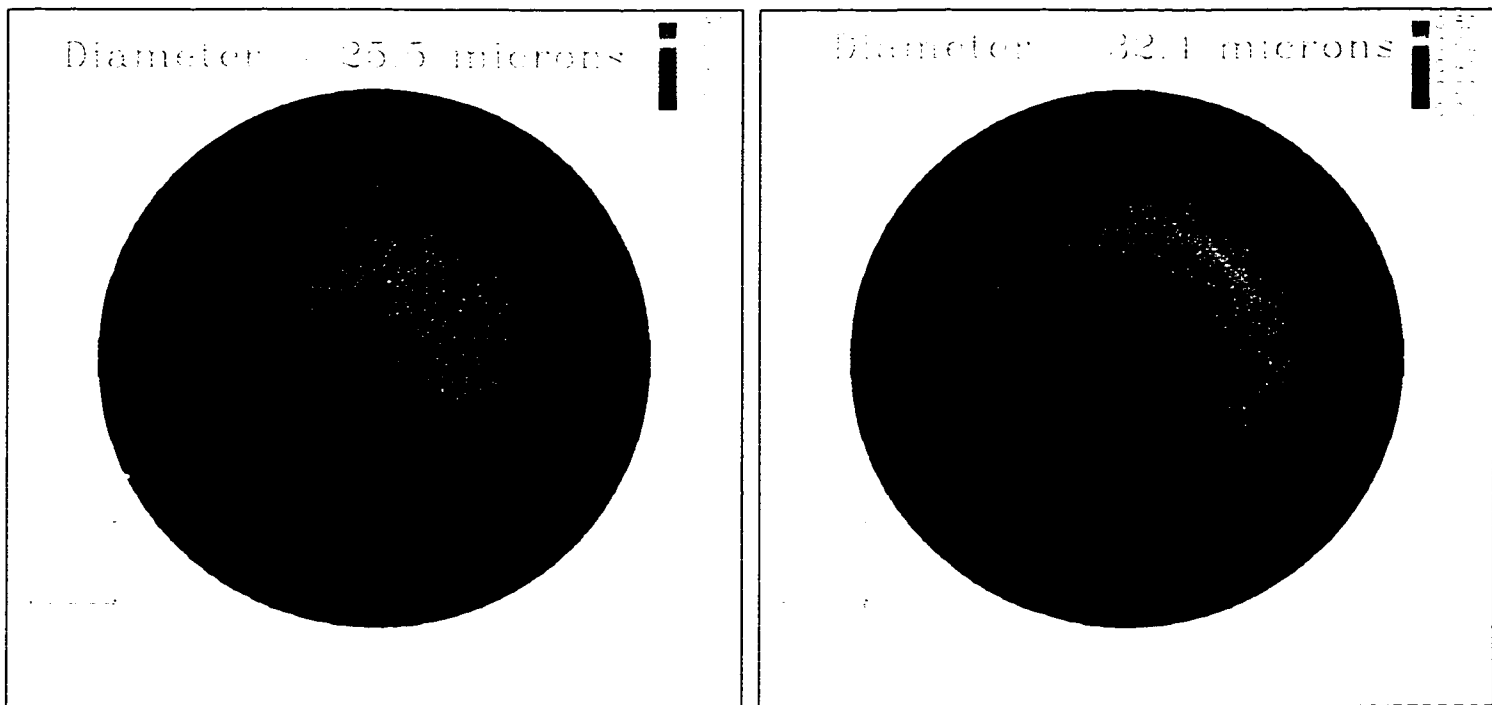


Figure 5.11: 15.04cm sphere surface collection efficiency for $d=25.5\mu m$ (left) and $d=32.4\mu m$ (right)

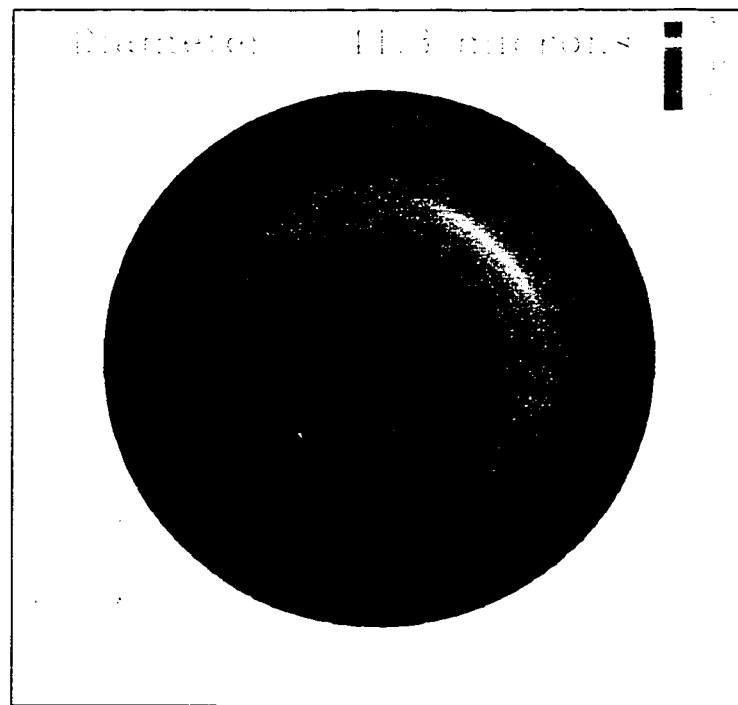


Figure 5.12: 15.04cm sphere surface collection efficiency for $d=41.3\mu m$

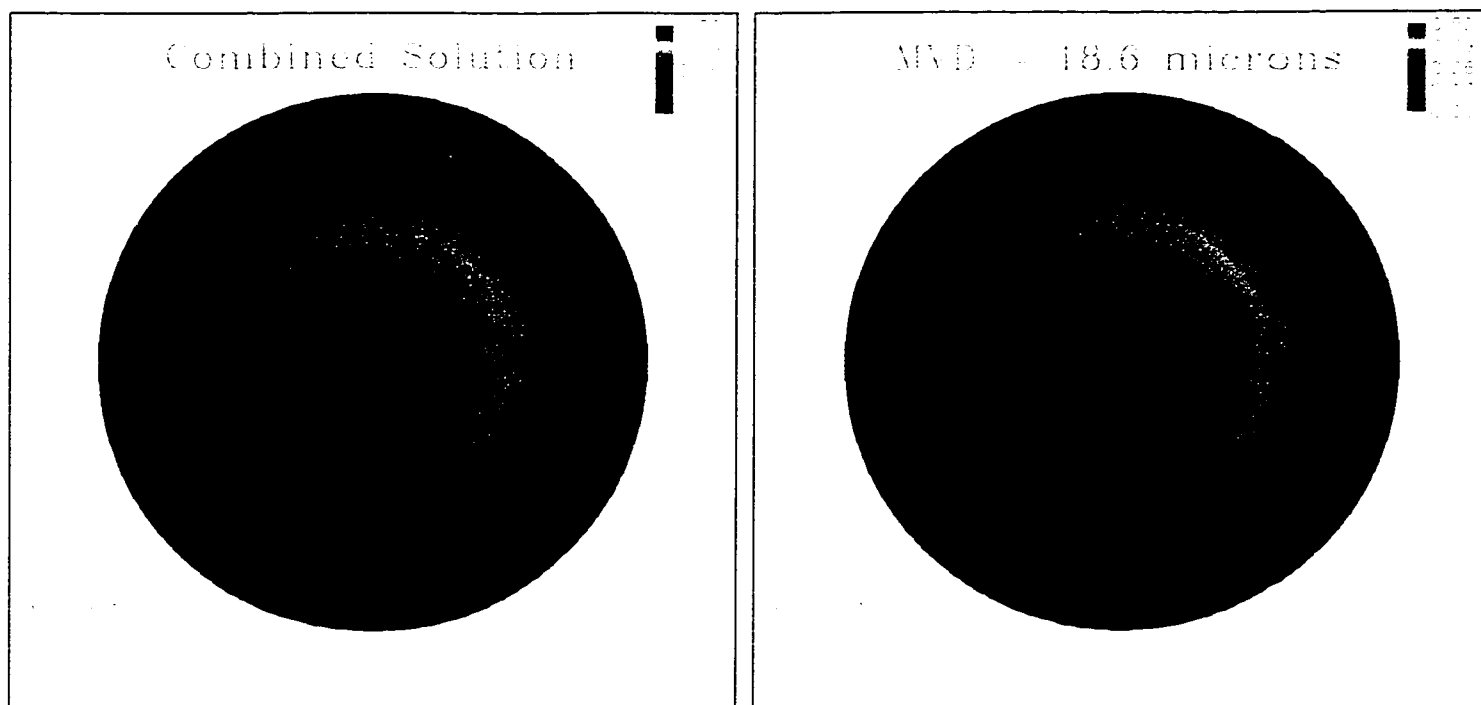


Figure 5.13: 15.04cm sphere surface collection efficiency for the combined solution (left) and the MVD = 18.6 μ m solution (right)

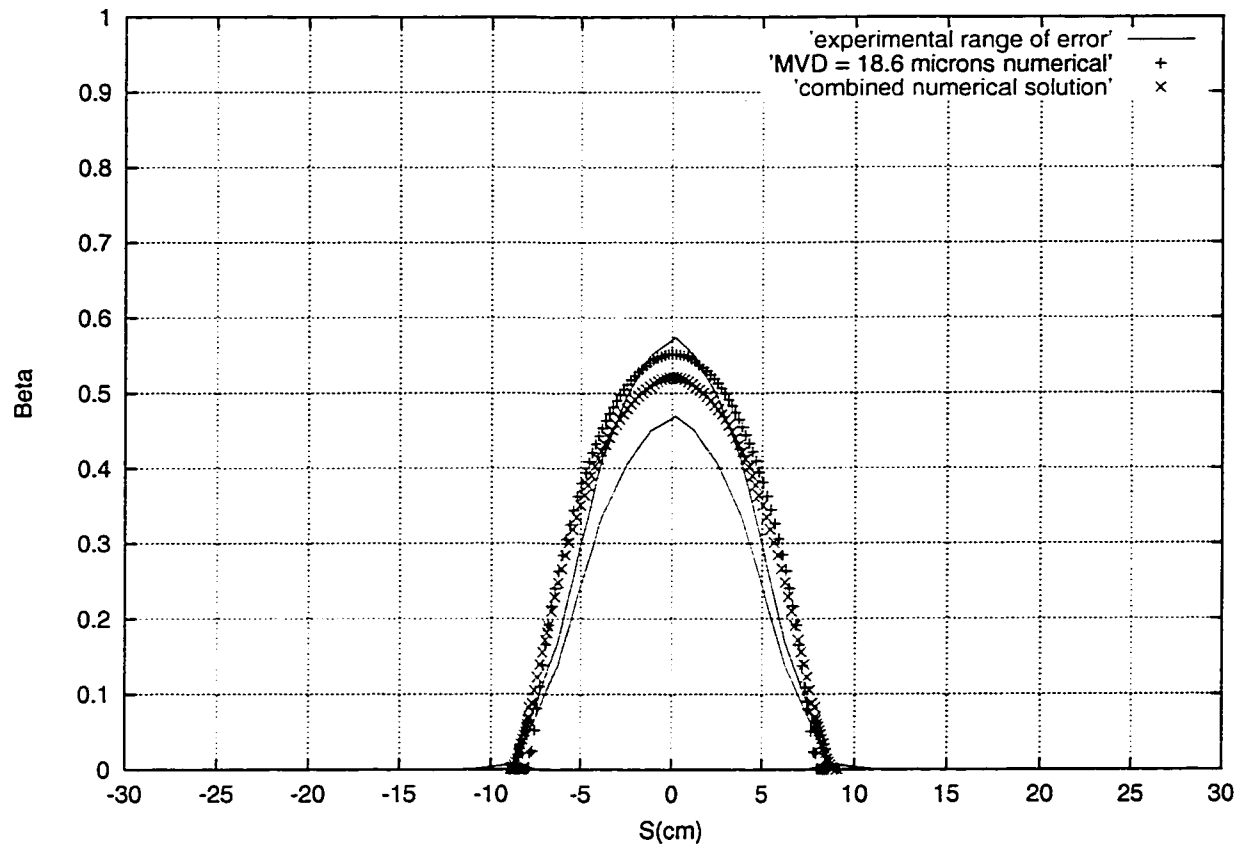


Figure 5.14: 15.04cm sphere surface collection efficiency vs. distance from the stagnation point

Chapter 6

Convair-580 Analysis

Chapter 4 gave a description of the Convair CAD model, the solution domain and the mesh used. Only an inviscid air flow solution was obtained for the Convair as a viscous solution would have necessitated more memory and CPU time than available within the time frame of this thesis.

6.1 Convair-580 Air Flow Solution

The flow input parameters for the Convair-580 inviscid solution were the following as provided by AES:

$M_{\infty} = 0.4$, the Mach number at infinity;

$T_{\infty} = 288.0^{\circ}K$, the static temperature at infinity;

$P_{\infty} = 1.0 \cdot 10^5 Pa$, the static pressure at infinity;

$R = 287.05 J/Kg.K$, the air gas constant;

$\gamma = 1.40$, the air specific heat ratio;

Fuselage AOA= 0° .

The static temperature and pressure values used are typical of sea level conditions and are believed to be suitable for this analysis. Above zero temperature was chosen in order to guarantee that no freezing was to be expected so that we would not have to compute an energy solution with the aerodynamic solution. Such values are considerable for our purposes since we are merely demonstrating the usability of the method for 3-D calculations over an airplane and side-window icing without any quantitative comparisons. Note that the static temperature's only effect on the air flow is in specifying the air flow velocity at infinity through the Mach number since the energy equation is not solved either in the air flow or the droplet flow. Thus the air flow velocity at infinity is

$$U_{\infty} = M_{\infty} \cdot \sqrt{\gamma \cdot R \cdot T_{\infty}} = 136.1 m/s$$

The surface pressure profile is shown in figure 6.1 with the pressure contours in the aircraft's longitudinal plane of symmetry. A noticeable effect is that of the windows recesses effect where local stagnation areas form, especially for the inside windows which directly face the flow. The mid and outside windows are relatively flush with the flow at 0° pitch roll and yaw so the pressure profile is unaffected since the air flow misses most of the windows recesses. Later on in the droplet analysis the windows recesses will be seen to have an important effect on impingement at the lower droplet diameters. The stagnation regions at the windows recesses can again be observed in figure 6.2 which is a close-up of the pressure profile at the windows.

The solution as shown in figures 6.1 and 6.2 displays some sensitivity with respect to the surface of the aircraft geometry. This is due to a slight misalignment of the b-spline surfaces forming the aircraft surface. Such a misalignment is due to the fact that the geometry was not initially available in CAD version and had to be constructed from blueprint measurements as mentioned in chapter 4. The data was presented in xyz format and included no information about surface characteristics which led to the above mentioned problems. This problem was, however, fixed at the windows where special care was taken

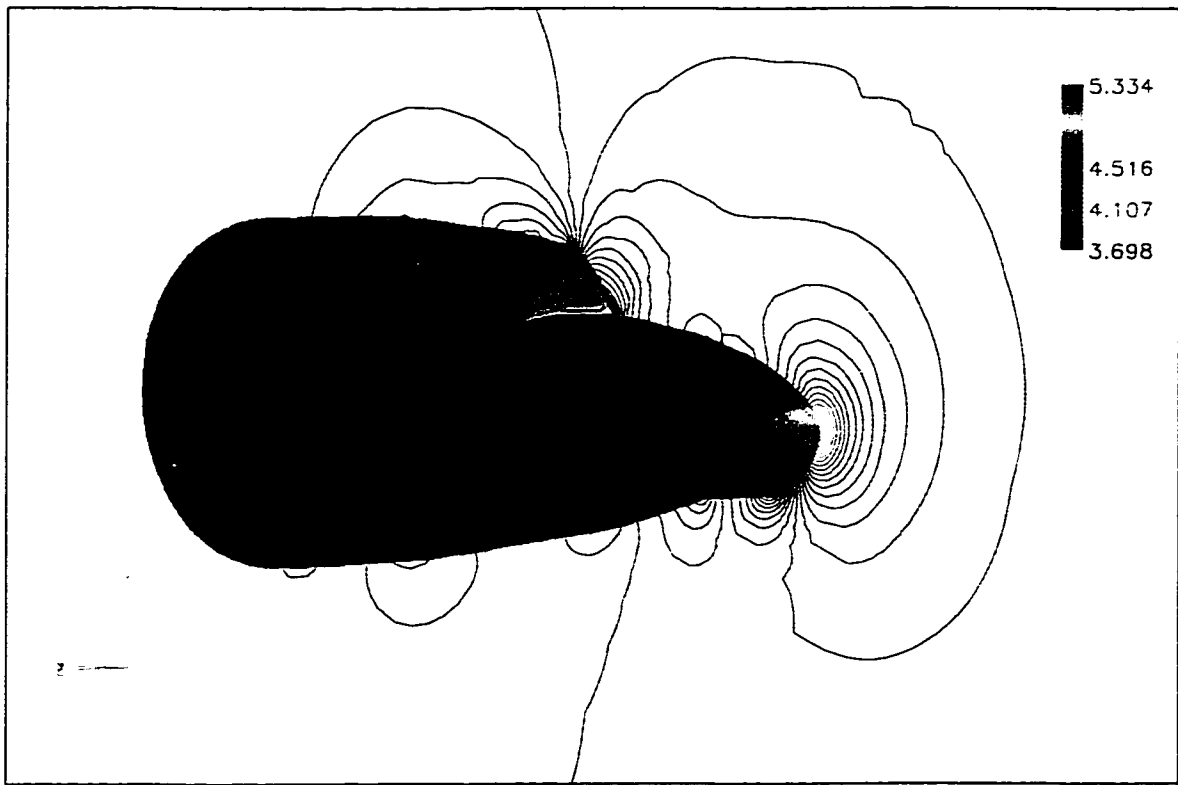


Figure 6.1: Surface pressure profile and pressure contours along the Convair's plane of symmetry

in insuring that the b-spline surfaces were well aligned together since the windows were the primary area of concern for AES.

6.2 Convair-580 Droplet Solutions

The same approach followed for the sphere's droplet solutions was followed for the Convair-580 where a number of droplet solutions at different required droplet diameters were calculated and combined to form a final solution. Eight droplet solutions were calculated for the Convair-580 based on the inviscid air flow solution discussed above. The droplet solutions were calculated at diameters of 10, 13, 20, 50, 100, 174, 200, 300, 400 and $1000\mu m$, a droplet distribution measured during one of the CFDE flights. The $1000\mu m$ solution, however, was calculated for the sole purpose of investigating the effect of large



Figure 6.2: Close-up of the surface pressure profile at the windows

droplets on collection efficiency on the side window. The droplet distribution is shown in figure 6.3 as LWC vs. droplet diameter. The overall LWC for this distribution is $0.137g/m^3$ and its MVD is $174\mu m$. The LWC weight for each diameter in the distribution was calculated by integrating under the LWC curve. These weights are shown in table 6.1.

The surface collection efficiency isolines on the Convair-580 geometry in front view are shown in figures 6.4, 6.5, 6.6, 6.7 and 6.8 for droplet diameters of 10, 13, 20, 50, 100, 200, 400 and $1000\mu m$ respectively. The solutions are truncated at a maximum surface collection efficiency value of $\beta = 1.00$. From figures 6.4 to 6.8 it can be observed that the impingement limits increase with increasing droplet diameters up to $400\mu m$. For 400 and $1000\mu m$ droplet diameters, the impingement limits seem to have stabilized or reached maximum values.

This same analysis can be confirmed in a quantitative manner by looking at cuts on the aircraft surface. A vertical cut and a horizontal one were selected on the aircraft surface and they are both shown in figure 6.10. From these cuts the surface collection efficiency was plotted for all the droplet diameters along the cut plane intersection with the aircraft surface. Figure 6.11 shows the surface collection efficiencies along the vertical cut for all the droplet diameters, as well as the combined distribution. As observed previously,

Table 6.1: LWC weights for the droplet diameters chosen to discretize the AES in-flight distribution

Percentage LWC	Ratio of Diameters	Droplet Diameter (μm)
9.9	0.06	10.0
8.8	0.09	13.0
14.5	0.11	20.0
5.6	0.29	50.0
5.6	0.57	100.0
8.3	1.00	174.0
12.5	1.15	200.0
19.9	1.72	300.0
15.0	2.30	400.0

the limits of impingement as well as the maximum values of collection efficiency increase with increasing droplet diameters. It is obvious from these results that most of the water collection is due to the higher diameter droplets. Moreover, the kink in the graph where the inside window edge is located demonstrates the edge effect in collecting more water than the planar part of the window. Figure 6.12 shows the collection efficiency on the Convair-580 surface along the horizontal cut which passes in the middle of the side window. The data displayed is the side window collection efficiency alone. It can be seen that the only appreciable impingement on the side window happens at droplet diameters of $300\mu\text{m}$ and above for which collection efficiencies are at least three times higher than the other droplet sizes. For diameters below $300\mu\text{m}$ the surface collection efficiencies along the side window are all nearly zero. The same edge effect seen for the inside window can be observed for the side window where kinks in the graphs at the window edge location indicate higher water collection for the edge than for the planar part of the window. Again we have seen that most water collection is due to the larger droplet. Thus, the percentage of the larger droplet in a droplet distribution would affect the overall collection efficiencies and water

collection at the surface. Such an effect can also be seen in the marked differences between a combined impingement solution obtained from the weighted contributions of all droplet classes in the profile and the MVD solution. The comparison was done in the same fashion as for the 2-D and 3-D test cases, and front views of both combined and MVD impingement profiles on the aircraft nose are shown in figure 6.9. The MVD for the AES flight segment was $174\mu m$. As expected from the validation results, the combined solution shows smaller peak impingement values and wider impingement limits. This is easily observed whether looking at the impingement profiles in figure 6.9 or the impingement coefficient curves from the horizontal and vertical cuts in figures 6.11 and 6.12. However, in the case of the aircraft the differences are much more pronounced between combined and MVD solutions reinforcing our conclusion that an MVD solution might not be representative of actual flow conditions especially in a real life case like the atmospheric cloud encountered during the CFDE flight segment and represented by the droplet diameters distribution in figure 6.3. Moreover, the side window shows almost no impingement for the MVD solution. The combined solution shows much more impingement than the MVD solution at the side window due to the larger droplet conferring an important role to SLDs in side window impingement.

No impingement measurements were available in order to compare with computational results. However, a photograph of an ice patch that accreted on the airplane's nose following a flight into a $300\mu m$ MVD cloud was provided following the completion of the calculations. Figure 6.13 shows the photograph side by side with the combined solution impingement profile on the nose of the Convair-580. We can see that the limits of the ice patch accretion zone and the Eulerian impingement zone on the nose are somewhat similar although the environmental conditions for the flight case at hand and the Eulerian solution were very different. This gives us added confidence in the capabilities of the Eulerian formulation in simulating droplet impingement on 3-D aircraft shapes.

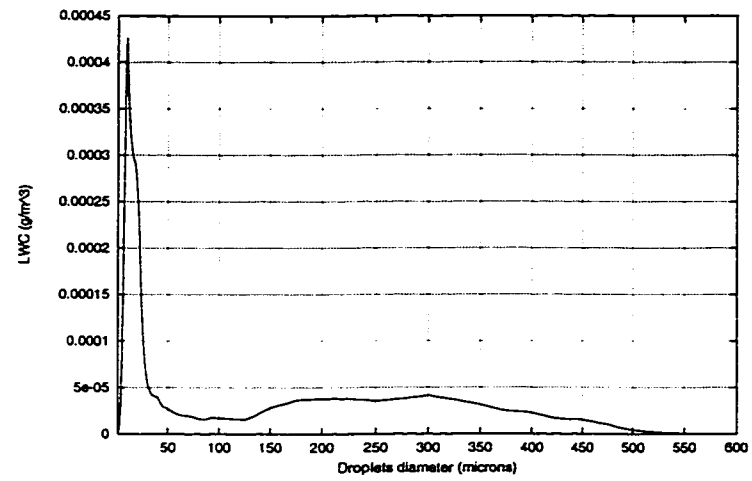


Figure 6.3: Droplet diameter distribution measured during a CFDE flight

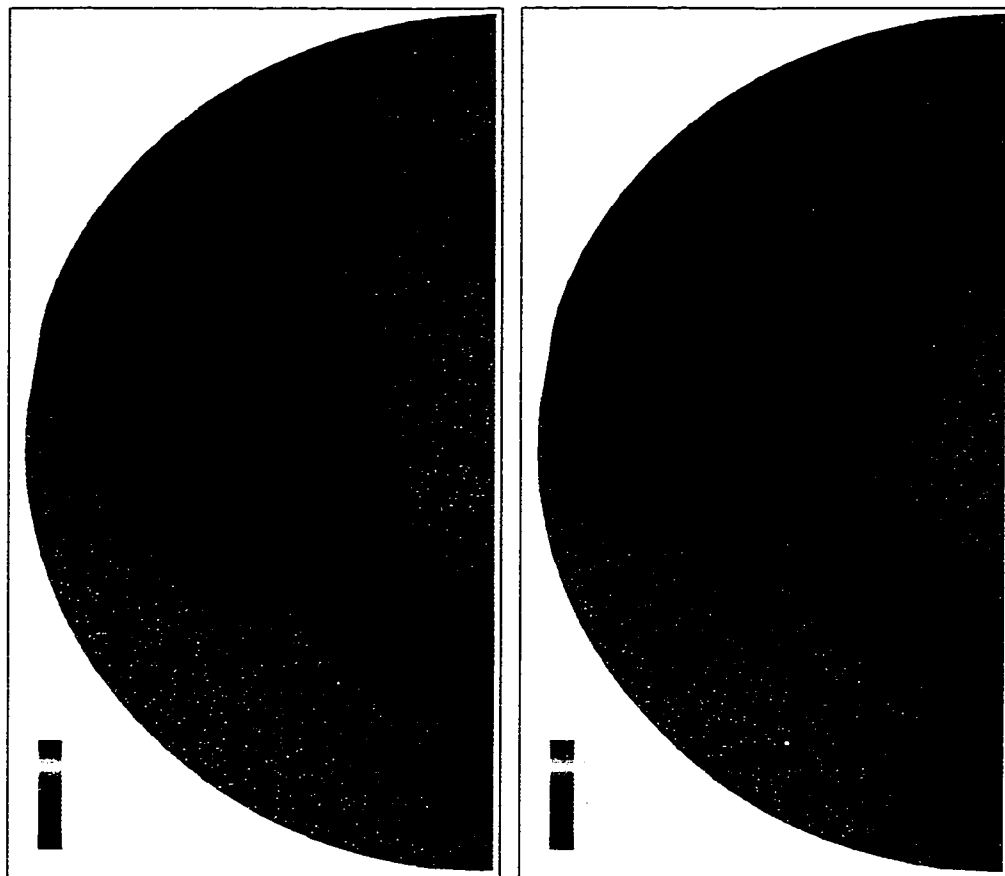


Figure 6.4: Front view of the Convair-580 surface collection efficiency for a droplet diameter of $10\mu m$ (left) and $13\mu m$ (right)

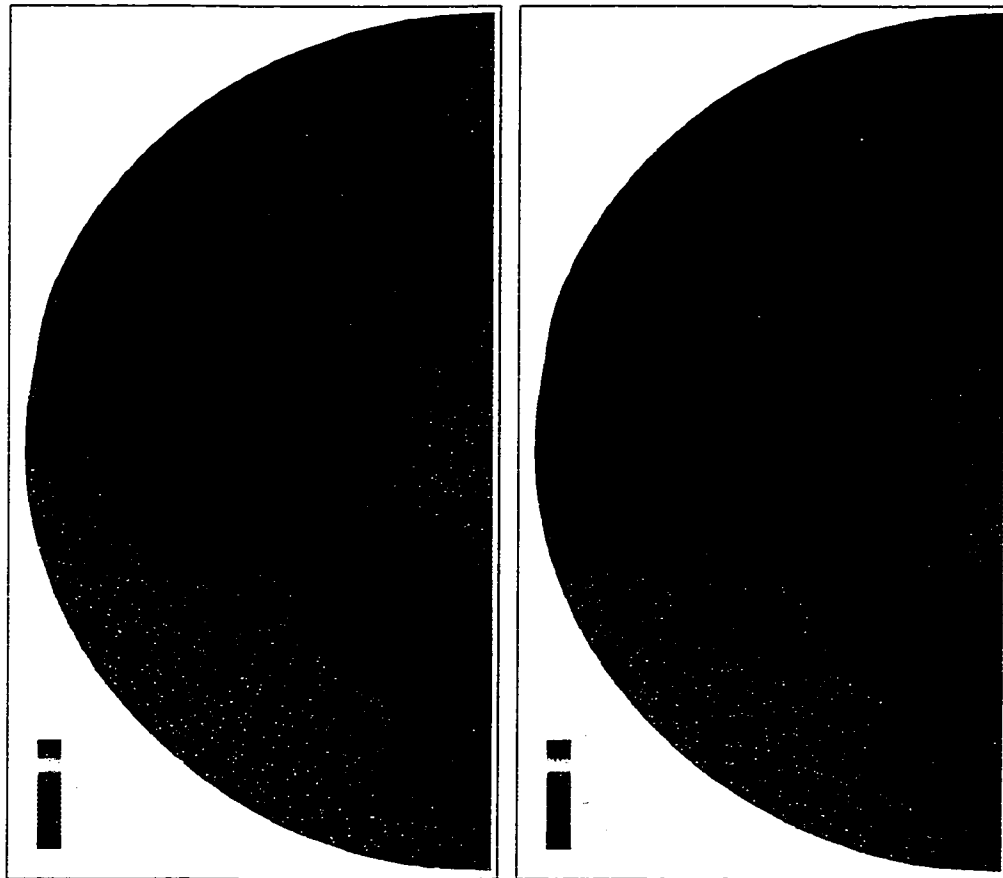


Figure 6.5: Front view of the Convair-580 surface collection efficiency for a droplet diameter of $20\mu m$ (left) and $50\mu m$ (right)

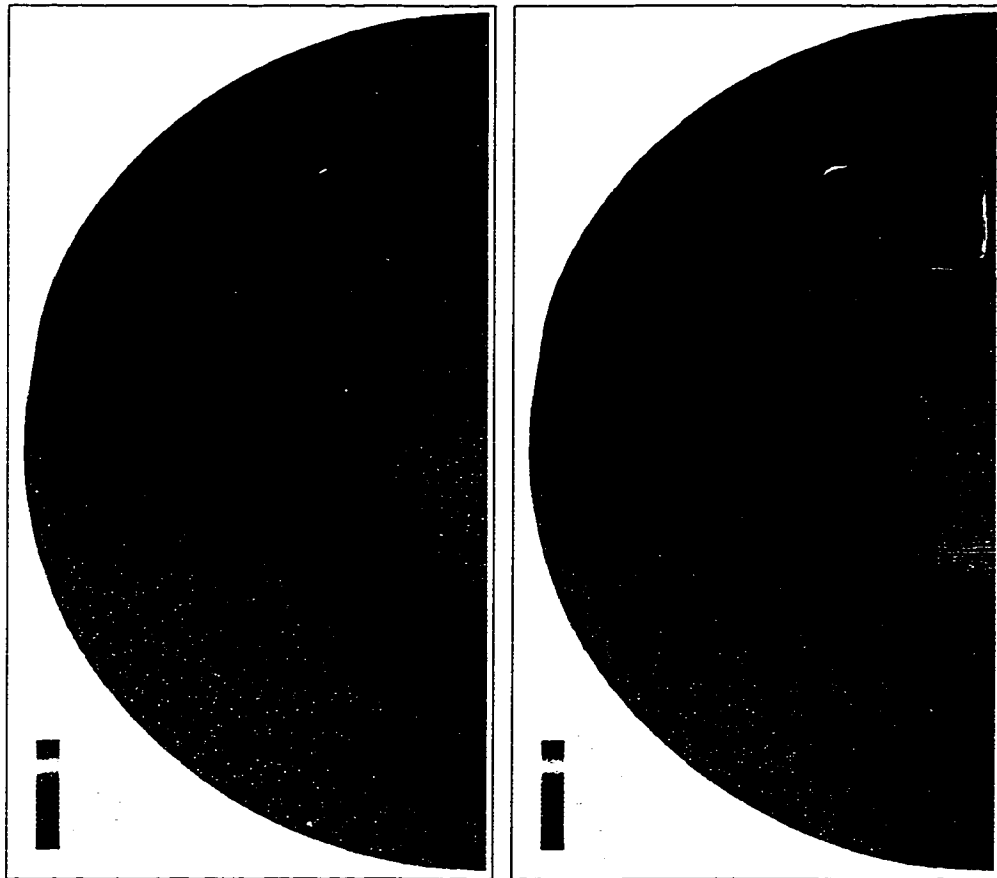


Figure 6.6: Front view of the Convair-580 surface collection efficiency for a droplet diameter of $100\mu m$ (left) and $200\mu m$ (right)

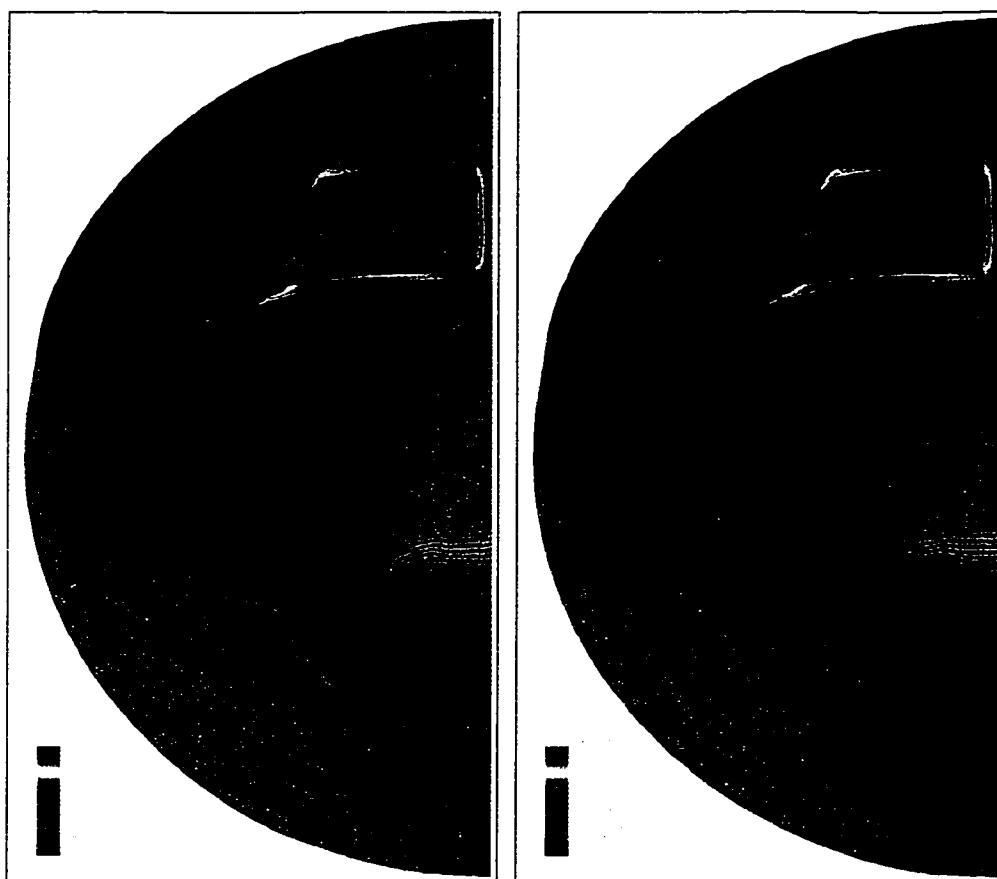


Figure 6.7: Front view of the Convair-580 surface collection efficiency for a droplet diameter of $300\mu m$ (left) and $400\mu m$ (right)

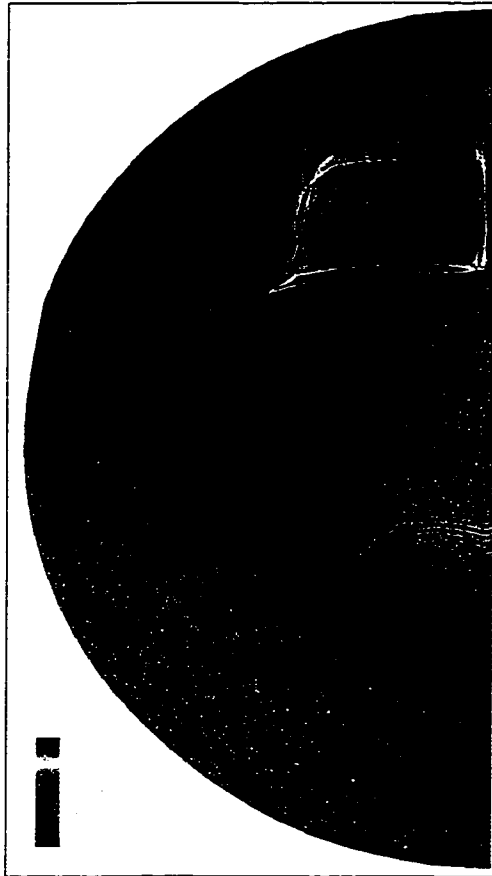


Figure 6.8: Front view of the Convair-580 surface collection efficiency for a droplet diameter of $1000\mu m$

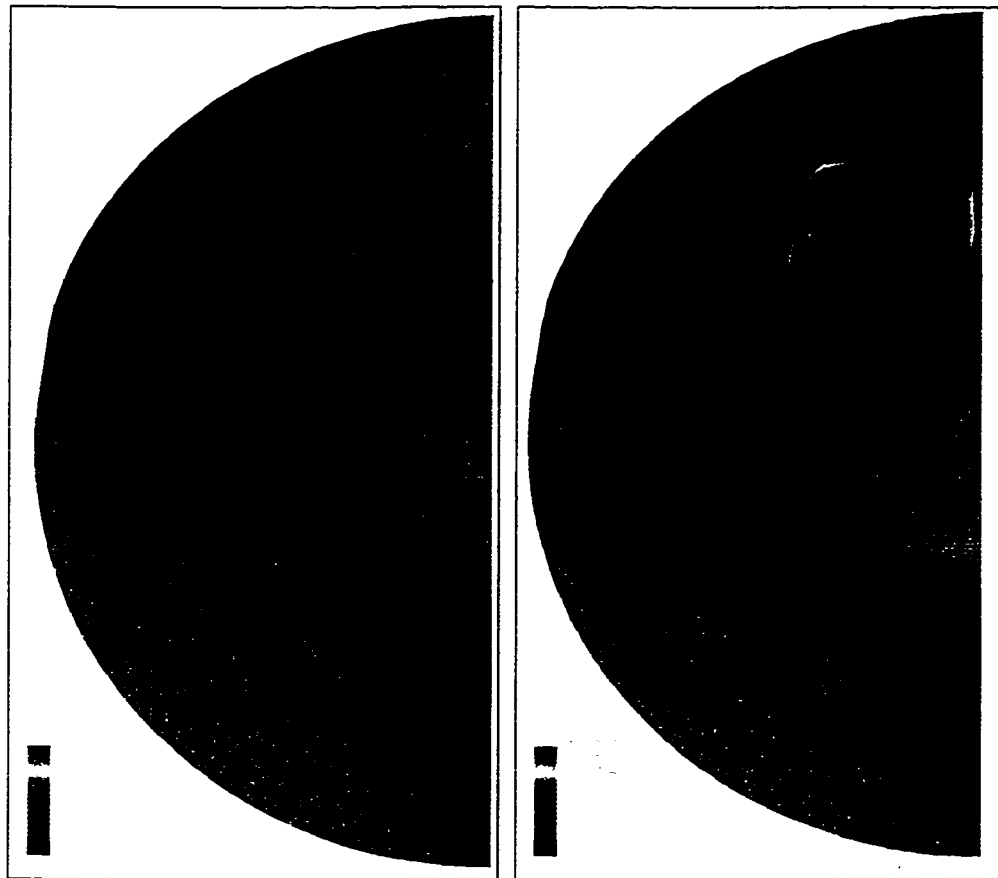


Figure 6.9: Front view of the Convair-580 surface collection efficiency for the combined solution (left) and the $MVD = 174\mu m$ solution (right)

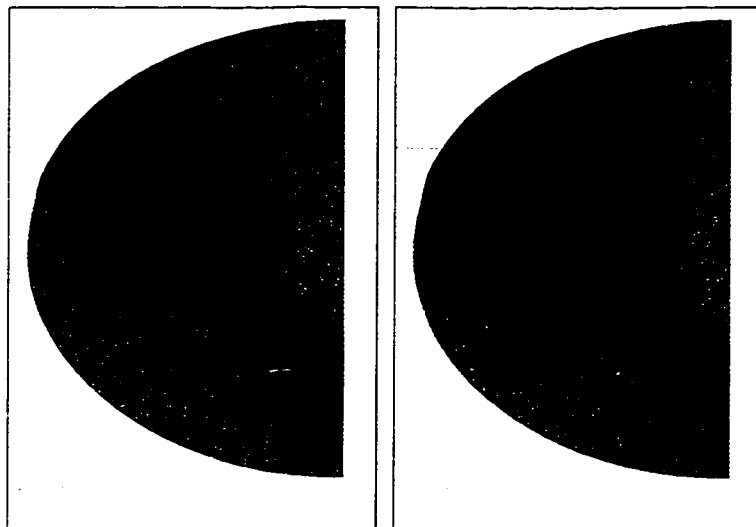


Figure 6.10: Vertical and horizontal cuts locations on the Convair-580 surface

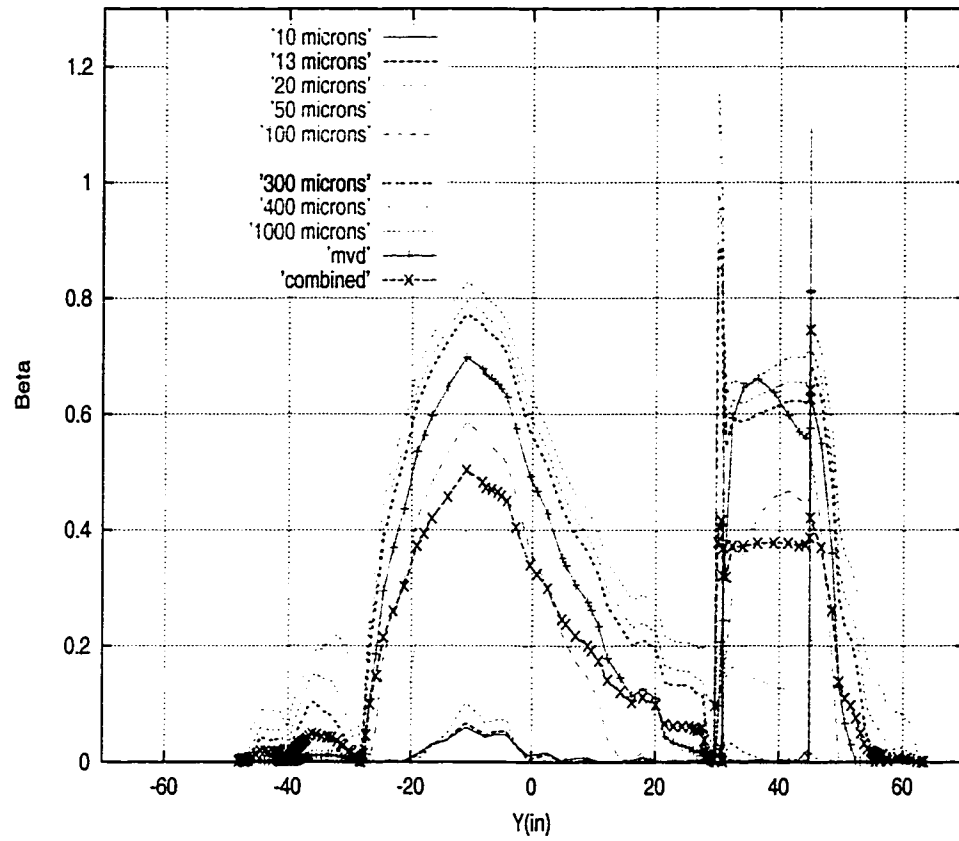


Figure 6.11: Collection efficiencies on the Convair-580 surface along a vertical cut

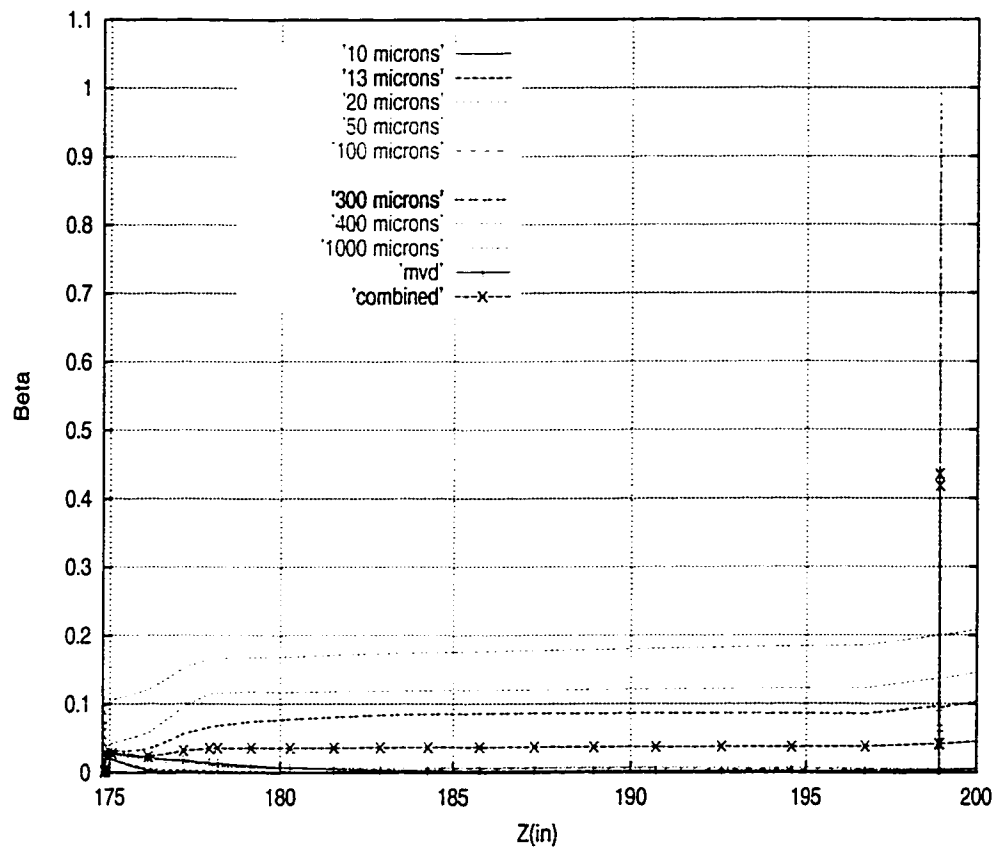


Figure 6.12: Collection efficiencies on the Convair-580 side window surface along a horizontal cut

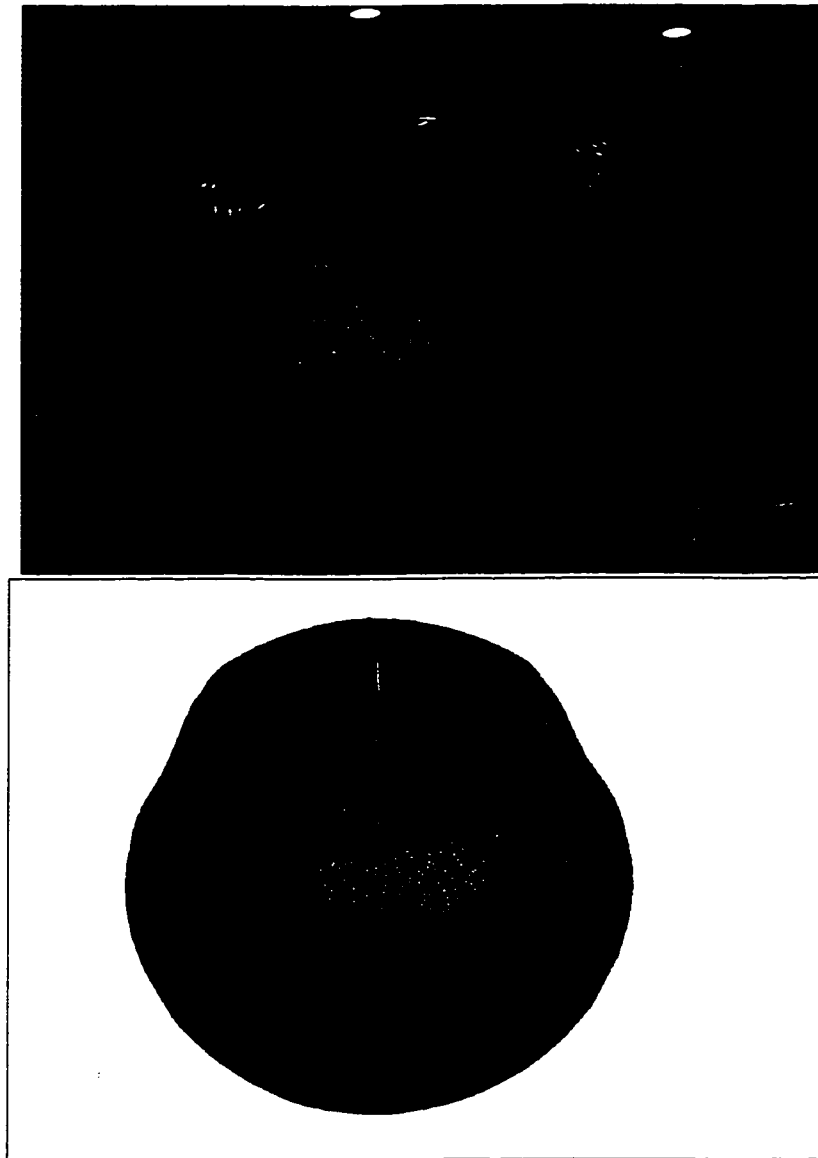


Figure 6.13: Comparison of the in-flight ice patch shape to the Eulerian impingement profile on the nose of the Convair-580

Chapter 7

Conclusions and Future Work

7.1 Conclusions

The Eulerian approach to droplet impingement calculation has been presented. FENSAP-ICE is the first modern icing code to use this approach in DROP3D its droplet impingement calculation module. DROP3D provides a droplet impingement solution for an arbitrary geometry by basing itself on a pre-calculated airflow solution. The airflow solution can be either inviscid or viscous laminar or turbulent. In fact, there are no restrictions over the type of airflow solutions that can be used. Of course, a judicious choice will undoubtedly reflect itself on the quality of the impingement solution.

DROP3D was successfully validated against published NASA experimental results. In fact, it was suggested that even better agreement with experimental data could be obtained if the actual icing tunnel experimental droplet diameter distributions were available instead of the assumed Langmuir-D distribution. We compared impingement solutions for one droplet diameter equal to the distribution's MVD to a combined solution of all the droplet diameters in the distribution. In both 2-D and 3-D modes we found better agreement with experimental data for the combined solutions than the MVD ones with the latter systematically over-estimating maximum impingement values and under-estimating impingement limits. These tendencies were more pronounced for the 3-D test-case than the 2-D one.

The Convair analysis was requested and funded by AES in order to investigate droplet impingement and side window icing on the Convair-580. The geometry coordinates were provided by AES and the CAD model as well as a hexahedral mesh for it were constructed at the CFD Laboratory using in-house facilities. A droplet diameters distribution was also provided by AES. This droplet distribution was measured during one of the CFDE flight segments. We selected several diameters throughout the distribution in order to approximate it. A droplet impingement solution was calculated for each of the diameters selected and a weighted combination of each solution was produced in order to compare with the MVD solution and analyze the results. This comparison produced the same conclusions as earlier with the validation test-cases. The MVD solution was again seen to produce narrower impingement limits and higher maximum impingement values. More importantly for the Convair analysis the MVD solution showed no impingement on the side window whereas the combined solution did. On the Convair the side window is the only one that's not heated. This means that when flying in icing conditions the side window is the only one that's likely to accrete ice. In the absence of ice accretion sensors on the airplane, side window icing could be a valuable way to determine whether the airplane is in SLD icing conditions or not. The individual droplet diameter solutions showed no impingement on the side window up till a droplet diameter of 300μ was reached. This result along with the fact that an MVD solution did not produce side window impingement whereas the distribution solution did means that side window impingement will occur in clouds of SLD with diameters well over 200μ for the Convair-580 in steady level flight. There were no experimental measurements available to verify this results but the success of the validations gives the Convair-580 analysis results a lot of confidence.

Overall, the Eulerian approach presents the following advantages over the Lagrangian one:

- No need to seed particles upstream of the geometry;
- No need for post-processing to obtain impingement coefficients as they are readily

available within the impingement solution;

- More confidence associated with the results since the formulation of the droplet phase flow through a set of partial differential equations guarantees results everywhere in the computational domain;
- The same formulation allows us to update the physics of the method with new terms as needed;
- The Eulerian method is typically suitable for problems with highly separated flows like wings with deflected control surfaces. These geometries are extremely hard to analyze (if not impossible) with Lagrangian codes but they present no particular challenge to the Eulerian approach. In essence we can say about the Eulerian approach that wherever an airflow solution can be obtained, so can a droplet impingement solution.

7.2 Future Work

All the cases considered in this thesis were satisfactorily treated with inviscid airflow calculations. However, some cases requiring turbulent airflow calculations such as wings with extended control surfaces might need to have the issues of droplets coalescence, breaking and splashing addressed. Moreover, the present formulation does not take into account the possible rebounding of droplets on solid surfaces and further research is desirable on this aspect as well. Most often, turbulent flows exhibit a transient nature or a repetitive pattern requiring a full transient treatment. It might be necessary to tighten the coupling between the airflow and droplet codes for such cases. Such tight coupling might even require formulating a two-fluid model where the airflow and droplet flow variables are computed simultaneously.

Bibliography

- [1] D.T. Bowden, A.E. Gensemer, and C.A. Skeen. "Engineering Summary of Airframe Icing Technical Data". Contract FA-WA-4250, Technical Report ADS-4, Federal Aviation Agency, Washington, D.C., 1964.
- [2] G.A. Ruff and B.M. Berkowitz. "Users' Manual for the NASA Lewis Ice Accretion Prediction Code (LEWICE)". Technical Report 185129, NASA, 1990.
- [3] T. Hedde. "Modélisation Tridimensionnelle des Dépôts de Givre sur les Voilures d'Aéronefs". Phd thesis, Université Blaise Pascal, France, 1992.
- [4] Y. Bourgault, W.G. Habashi, J. Dompierre, and G. Baruzzi. "A Finite Element Method Study of Eulerian Droplets Impingement Models". International Journal of Numerical Methods in Fluids. To appear in 1999.
- [5] S.G. Cober, J.W. Strapp, and G.A. Isaac. "An Example of Supercooled Drizzle Drops Formed Through a Collision-Coalescence Process". Journal of Applied Meteorology, 1996, pp. 2250-2260.
- [6] S.G. Cober, G.A. Isaac, and J.W. Strapp. "Aircraft Icing Measurements in East Coast Winter Storms". Journal of Applied Meteorology, 1995, pp. 88-100.
- [7] A. Tremblay, S.G. Cober, A. Glazer, and G.A. Isaac. "Observations and Parametrization of Mixed-Phase Clouds During the Canadian Freezing Drizzle Experiment". Proceedings of the 12th Intl. Conf. on Clouds and Precipitation, August 1996, pp. 835-838, Zurich, Switzerland.

- [8] D.L. Marcotte, J.W. Strapp, S.G. Cober, and G.A. Isaac. "The NRC Convair-580 Research Aircraft: Configuration in the Canadian Freezing Drizzle Experiment". Proceedings of the FAA International Conference on Aircraft Inflight Icing, May 1996, vol. II, pp. 125-135, Springfield, Virginia.
- [9] Z. Boutanios, Y. Bourgault, W.G. Habashi, G.A. Isaac and S.G. Cober. "3D Droplets Impingement Analysis around an Aircraft's Nose and Cockpit using FENSAP-ICE". AIAA conference paper 98-0200, January 1998, Reno, Nevada.
- [10] Y. Bourgault, W.G. Habashi, J. Dompierre, G. Baruzzi, and G. Chevalier. "An Eulerian Computational Approach to Ice Droplets Impingement". Computational Fluid Dynamics Conference, September 1996, Paris, France.
- [11] C.T. Crowe. "Review-Numerical Models for Dilute Gas-Particle Flows". Transactions of the ASME, Journal of Fluids Engineering, vol. 104, pp. 297-303, 1982.
- [12] G.S. Baruzzi. "A Second Order Finite Element Method for the Solution of the Transonic Euler and Navier-Stokes Equations". Phd thesis, Concordia University, Montreal, Canada, 1995.
- [13] G. Guèvremont. "Finite Element Vorticity-Based Methods for the Solution of the Incompressible and Compressible Navier-Stokes Equations". Phd thesis, Concordia University, Montreal, Canada, 1993.
- [14] J. Dompierre, M.-G. Vallet, M. Fortin, Y. Bourgault and W.G. Habashi. "Anisotropic Mesh Adaptation: Towards a Solver and User Independent CFD". AIAA conference paper 97-0861, January 1997, Reno, Nevada.
- [15] T.J.R. Hughes and M. Mallet. "A New Finite-Element Formulation for Computational Fluid Dynamics: III. The Generalized Streamline Operator for Multidimensional Advective-Diffusive Systems". Computer Methods in Applied Mechanics and Engineering, vol. 58, pp. 305-328, 1986.

- [16] T.J.R. Hughes, M. Mallet and A. Mizukami. "A New Finite-Element Formulation for Computational Fluid Dynamics: II. Beyond SUPG". Computer Methods in Applied Mechanics and Engineering, vol. 54, pp. 341-355, 1986.
- [17] P. Brown and Y. Saad. "Hybrid Krylov Methods for Nonlinear Systems of Equations". Technical Report UCRL-97645, Lawrence Livermore National Laboratory, November 1987.
- [18] C. Lepage and L. Dutto. "A Guide to FENSAP, Version 4.10". CFD Laboratory, Department of Mechanical Engineering, Concordia University, January 8, 1999.
- [19] C.S. Bidwell and Jr S.R. Mohler. "Collection Efficiency and Ice Accretion Calculations for a Sphere, a Swept MS(1)-317 Wing, a Swept NACA-0012 Wing Tip, an Axisymmetric Inlet, and a Boeing 737-300 Inlet". AIAA conference paper 95-0755, January 1995, Reno, Nevada.
- [20] J.D. Reichhold, M.B. Bragg, and D. Sweet. " Experimental Determination of the Droplet Impingement Characteristics of a Propeller". AIAA conference paper 97-0179, January 1997, Reno, Nevada.